Spring 2009

Interference effects due to projective-target nucleus scattering in single ionization of molecular hydrogen by 75 keV proton impact

Jason S. Alexander

Department: Physics

INTERFERENCE EFFECTS DUE TO PROJECTILE – TARGET NUCLEUS SCATTERING IN SINGLE IONIZATION OF MOLECULAR HYDROGEN BY 75 KEV PROTON IMPACT

by

JASON S. ALEXANDER

A DISSERTATION

Presented to the Faculty of the Graduate School of the

MISSOURI UNIVERSITY OF SCIENCE AND TECHNOLOGY

In Partial Fulfillment of the Requirements for the Degree

DOCTOR OF PHILOSOPHY

in

PHYSICS

2009

Approved by

Michael Schulz, Advisor
Don Madison
Robert Dubois
Greg Story
Kimberly Henthorn

ABSTRACT

Doubly-differential cross-sections for the single ionization of molecular hydrogen by 75 keV proton impact have been measured as a function of the projectile scattering angle and energy loss and compared to available theoretical models. Interference structures are directly observed in the scattering angular dependence of the DDCS. The phase angle appears to be most sensitive to the projectile angle but not as sensitive to the electron energy, suggesting that the projectile - target nucleus interaction plays a central role in the interference. The large-angle structures disappear at electron speeds near the projectile speed. This may be due to a focusing effect introduced by post-collision interaction. Furthermore, our data suggest that for a given scattering angle, the ionization amplitude depends strongly on the molecular orientation, relative to the projectile beam axis, with transverse orientation favored at small angles and longitudinal orientation at large angles.

ACKNOWLEDGMENTS

I would like to thank my advisor, Dr. Michael Schulz, for giving me the opportunity to continue to learn exciting physics and for teaching me about collision physics, data analysis, and scientific diplomacy. I am forever in your debt. I would also like to thank the other members of my committee for their time and effort. I would also like to thank Drs Z.S. Machavariani, M.F. Ciappina, R.D. Rivarola, and D.H. Madison, for their theoretical collaboration for comparison to and support of interpretation of the data, and Dr. Ahmad Hassan for fruitful discussions at the beginning of this experiment. Thank you to Dr. J.M. Paikeday of Southeast Missouri State University for getting me interested in atomic physics so long ago as an undergraduate and to Drs Eric Abraham, Neil Shafer-Ray, and Michael Morrison of the University of Oklahoma for their continued support of my endeavors. I would also like to thank my fellow graduate students in the Schulz' lab, Kisra and Aaron, for their hard work. I want to thank Charlie McWhorter, Russ Summers, Pam Crabtree, and Ellen Kindle for all of their help. Jared Gavin, Elizabeth Black, and especially Mark and Mary Thomason made my time in Rolla enjoyable both inside and outside of physics. I also want to thank those who have been tremendous friends throughout my higher education: Laura Ernst and Wendy Johnson and their spouses Nathan and Everett, K.V. Shajesh, and Prachi Parashar for being supportive all of these years and letting me have good times when I needed them most, thank you. I want to thank my parents for sacrificing so that I could get to the point in life I am today and my brothers for always believing in me more than I did myself. Finally, words are inadequate to express how happy I am to have Jennifer and Clay on this journey with me.

TABLE OF CONTENTS

LIST OF ILLUSTRATIONS

Figure Page

LIST OF TABLES

NOMENCLATURE

Atomic units are frequently used in this dissertation. Therefore, some important physical quantities in atomic units along with their SI or CGS conversion factor are listed here. The mass, charge, action, and permittivity are the only independent atomic units.The remainder are derived from combinations of these units. An excellent review of atomic units and their use may be found in Appendix F of [1].

Quantity	Name	Symbol	Value in SI/CGS
mass	electron rest mass	m_e	9.109×10^{-31} kg
charge	electron charge	e	1.602×10^{-19} C
action	reduced Planck's constant	$\hbar = h/(2\pi)$	1.054×10^{-34} J s
permittivity		$\kappa_o = 4\pi\epsilon_o$	1.112×10^{-10} F/m
energy	Hartree	$E_h = m_e e^2/(\kappa_o \hbar^2)$	27.211 eV
fine structure const.		$\alpha = e^2/(\kappa_o \hbar c)$	1/137.036
length	first Bohr radius	$a_o = \hbar/(m_e c \alpha)$	5.291×10^{-11} m

1. INTRODUCTION

The fundamental understanding of nature involves solving two problems. First is the comprehension of the four fundamental forces. These forces are mediated by the exchange of particles, the gauge bosons. This is essentially a two-body process because a gauge boson can only be emitted and absorbed by one particle at a time. This leads directly to the second problem that needs to be solved: discerning the spatial and temporal evolution of a system of more than two particles under the influence of these pair-wise acting forces. It can be shown that the Schrödinger equation is not analytically solvable for more than two mutually interacting particles, even if the underlying forces are exactly known. Consequently, theory has to resort to extensive modeling using approximations, the validity of which must be tested experimentally. This is known as the few-body problem and is one of the most important unsolved problems in physics.

Atomic and molecular collisions are particularly well suited to the study of the fundamental few-body problem [2-4]. In an atomic or molecular collision experiment the underlying interaction, the electromagnetic force, is well understood. This is in contrast to nuclear processes, in which the forces are not as well understood. As a result, an atomic or molecular collision experiment provides a direct test of the theoretical description of the few-body aspects. However, for a nuclear collision system it is not clear whether experiment tests the few-body aspects or the description of the underlying forces.

In addition to knowledge of the underlying force, the particle number involved in atomic or molecular collisions can be kept small. In the last decade [5] experimental techniques have been developed so that the momentum components of all of the particles in the system can be completely determined for systems containing up to five particles. These types of experiments are therefore said to be kinematically complete. In contrast, in a solid-state system, for example, it is clearly impossible to measure the momentum components of all the particles in the system (on the order of Avogadro's number). Therefore, for such systems only statistically averaged or collective quantities can be measured. Clearly, these measurements do not provide as sensitive a test of theory as atomic or molecular collision experiments. Thus in kinematically complete atomic collisions experiments, any discrepancies between theory and experimental data can be attributed to the description of few-body effects in the theoretical model. Ionizing collision processes are particularly suitable because, unlike capture or excitation, the final state involves at least three unbound particles in the continuum interacting with Coulomb interactions.

Multiple differential single ionization cross-sections for atomic targets have been measured for a wide range of collision systems. For small perturbations η, the projectile charge-to-velocity ratio, and simple atomic targets, a qualitative understanding of the reaction dynamics has begun to emerge [6]. However, for increasing perturbation serious discrepancies between theory and experiment remain [7]. Theoretical difficulties not only increase with increasing perturbation, but also with increasing target complexity. For example, for heavy atomic targets that have many electrons agreement between theory and experiment is considerably worse than for light target atoms [7].

For molecular targets, the complexity of the electronic wave-function makes theoretical analysis more cumbersome. Conversely, the two (or multiple) center potential of the molecule also makes it more interesting. For example, since one cannot distinguish from which center the scattered projectile wave is diffracted, both contributions need to be treated coherently which may lead to observable interference patterns. These interference effects provide an interesting and sensitive avenue for the investigation of few-body dynamics.

Interference structures in collisions with molecular targets were first suggested by Tuan and Gerjouy [8] in theoretical calculations of charge transfer cross-sections, $p + H_2 \rightarrow H + H_2^+$ in proton collisions with molecular hydrogen. In that work, the inability to determine which proton in the molecule the captured electron is associated with leads to a phase factor, in accord with elementary diffraction theory for two identical scattering centers with a fixed relative displacement. Cohen and Fano [9] examined interference effects in the ejected electron in the photo-ionization of molecules and the specific case of H_2^+ in detail. In that work an interference term in the total ionization cross-section of the form $1 + \frac{\sin(\boldsymbol{k}\cdot\boldsymbol{r})}{\boldsymbol{k}\cdot\boldsymbol{r}}$,was predicted, where **k** is the momentum of the ionized electron.

Experimentally, structures that were attributed to interference effects in the ejected electron wave-function were first reported in double differential ionization cross-sections, $d^2\sigma/d\Omega_e dE_e$, differential in the ejected electron energy and angle, in single ionization of the simplest neutral molecular system, H_2, by fast ion impact [10]. Such structures have since been reported in further studies of double differential ionization cross-sections by ion impact [11, 12, 13], fully differential cross-sections for ionization

by electron impact [14, 15], as well as in the double photo-ionization of H_2 [16]. In [10] cross-sections differential in the ejected electron energy and emission angle were presented in 60 MeV/u Kr^{34+} collisions with H_2 for electron energies in the range 2-300 eV. It has been shown that to a good approximation the triply differential cross-section sections $d^3\sigma/d\Omega_p d\Omega_e dE_e$ (TDCS) for H_2 averaged over all molecular orientations can be expressed in terms of the TDCS for atomic hydrogen by [10, 17, 18]:

$$\mathrm{TDCS}_{H_2} = 2\mathrm{TDCS}_{H}\left[1+\frac{\sin(\chi)}{\chi}\right] \quad (1)$$

Here, the phase factor in the interference term $1+\frac{\sin(\chi)}{\chi}$ is $\chi = p_{rec}D$, where p_{rec} is the magnitude of the recoil-ion momentum, and D is the internuclear distance in the molecule.

In analyzing the doubly-differential cross-sections $d^2\sigma/d\Omega_e dE_e$ **,** Stolterfoht et al [10, 11] assumed that the momentum transfer to the target **q** was negligible and set it to zero, so that the approximation, $|\mathbf{p}_{\mathrm{rec}}| = |\mathbf{q} - \mathbf{k}_{\mathbf{e}}| \sim k_e$ was made. In equation (1) the TDCS can then be replaced by the DDCS. No interference structures were observed directly in the double differential cross-sections, and only after normalizing the molecular cross-sections to theoretical cross-sections for atomic hydrogen was a weak structure obtained. These structures were interpreted as interference in the ejected electron wave-function due to the coherent emission of the electron from each of the atomic centers. Hossain et al followed the same procedure as [10] in analyzing collisions of 3-5 MeV protons with H_2 [12], again interpreting any structure in the molecular to theoretical atomic cross-section ratios as due to coherent emission of the electron from the two

atomic centers. Misra et al. measured cross-sections differential in ejected electron energy and angle in single ionization of H_2 by 1.5 MeV/u F^{9+} and 1 MeV/u C^{6+} impact [13]. In that work the cross-sections were also measured for atomic hydrogen and the ratios of the experimental cross-sections, molecular to atomic, were presented. In contrast to the data of Stolterfoht et al. [10, 11] and Hossain et al. [12], this experiment had the advantage that theoretical uncertainties in the atomic cross-sections are removed by having measured both cross-sections in the ratio. Oscillatory structures were found only in the ratios and were again interpreted as an interference in the coherent emission of the electron. However, the fact that only weak structures were obtained in the ratios of the molecular to atomic cross-sections and not at all directly in the molecular cross-sections undermines the conclusion that they represent an interference effect. Structures unrelated to interference can easily be produced in cross-section ratios. For example in the ratio of double to single ionization cross-sections, structures are generated due a difference in the rate of change in slope of the cross-sections [19].

Similar double differential cross-sections, differential in ejected electron energy and angle, for 80 MeV C^{6+} impact were measured by Misra et al. [20]. In that work the authors analyzed the experimental data in terms of an asymmetry parameter α(k), defined by,

$$\alpha(k) = \frac{\sigma(k,\theta_1)-\sigma(k,\theta_1-\pi)}{\sigma(k,\theta_1)+\sigma(k,\theta_1)} \quad (2)$$

where the ejected electron energy is $\varepsilon_k=k^2/2$ in a.u. and θ_1 is chosen to be a small forward angle (20°). Based on theoretical studies by Fainstein et al [21], this parameter was

expected to exhibit a forward-backward angular asymmetry in low-energy electron emission by ion impact. Misra et al found oscillations in the experimentally determined asymmetry parameter, which were interpreted as interference in the ejected electron wave-function. Because this analysis is independent of any cross-section ratio it can be considered as the first convincing experimental evidence for interference in the ejected electron wave-function in single ionization of a molecular target by charged particle impact.

In analyzing triple differential cross-sections due to electron impact ionization of H_2, Casagrande et al [22] pointed to oscillations in ratios to measured helium cross-sections to indicate interference due to the same coherent electron emission mechanism. In that work the cross-section ratios were plotted for fixed projectile scattering angle and electrons with fixed energy ejected into the scattering plane as a function of the electron ejection angle. This data, in comparison to that of Stolterfoht et al [10, 11] and Hossain et al [12] suggest that the phase angle depends on both the ejected electron energy and angle. Here too, no structure is directly observed in the molecular cross-sections and the interpretation of an interference relies solely on cross-section ratios between H_2 and an atomic target. In this instance, using an atomic target, helium, represents an even greater uncertainty because helium differs from H_2 even more than atomic hydrogen in binding energy and in the initial electron position distribution.

Finally, D. Akoury et al [16] demonstrated interference in the ejected electron wave-function in the double photo-ionization of H_2, and a decoherence resulting from the interaction of one electron with the Coulomb field of the other ejected electron.

In Eq. (1), the phase angle χ present in the interference term basically depends on three quantities: the molecular orientation, the electron momentum $\mathbf{k_e}$, and the momentum transfer **q** from the projectile to the target. It has been shown [17] that averaging over the molecular orientation does not completely destroy the interference pattern. However, integration over **q,** which is inherent to the double differential electron spectra measured in [10, 11, 12], may suppress the phase factor such that an interference pattern is not readily observable in the absolute cross-sections. On the other hand, double differential cross-sections as a function of **q**, or equivalently the projectile scattering angle and ejected electron energy, are not integrated over **q**, but instead over the ejected electron solid angle. If the phase angle is more sensitive to **q** than it is to $\mathbf{k_e}$, it is possible that an oscillating interference pattern is more pronounced in such cross-sections.

As stated above, the analysis of the asymmetry parameter in the work of Misra et al [20] is independent of any cross-section ratio therefore it can justifiably be viewed as the first convincing experimental evidence for interference in the ejected electron wave-function in single ionization of a molecular target by charged particle impact. However, there is no previous experimental evidence to indicate interference in the scattered projectile wave-function in single ionization of molecular targets by charged particle impact. In this dissertation, measured doubly differential cross-sections for single ionization of H_2 by 75 keV proton impact as a function of the scattered projectile angle, θ, and ejected electron energy, E_e, are presented. In stark contrast to previous work looking at the ejected electron wave-function [10-15], prominent interference structures are observed directly in the projectile scattering angle dependence, without any normalization to atomic cross-sections. These structures are related to coherent scattering

between the projectile proton and the residual target nuclei. The data are then compared to the data available from various theoretical models and it is demonstrated that the projectile-target nucleus interaction plays a pivotal role in the interference. In addition, the data strongly suggest, for the first time, that the ionization amplitude does indeed depend strongly on the molecular orientation.

2. THEORETICAL MODELS

2.1. OVERVIEW

In order to describe the dynamics of an atomic or molecular collision the Schrödinger equation must be solved. However, as discussed in Section 1.1, this is analytically impossible for more than two mutually interacting particles, even though the fundamental interaction, the electromagnetic interaction, is well understood. As a result, numerous models have been developed which include the underlying physics in various approximation schemes and to varying degrees.

One way in which the theoretical description of few-body dynamics can be investigated with great sensitivity is by studying interference phenomena. The situation is analogous to a Young's double slit. Consider a projectile with initial momentum $\mathbf{p_o}$ incident on a molecule with nuclei separated by a fixed distance, D (refer to Fig. 1.1). The molecular axis makes an angle α with the initial beam axis and a detector is placed at an angle θ with respect to the beam axis. Regard the projectile proton as an incoming de Broglie wave, with wavelength $h/p_0 \sim 1.98 \times 10^{-3}$ au. Because it cannot be determined from which nuclei the projectile de Broglie wave scattered, the scattering amplitudes must be added coherently, which leads to an interference. Continuing with the optical analogy, the coherent triple differential scattering cross-section is represented as an incoherent part times an interference term, $\mathcal{I}$.

$$d^3\sigma_{coh} = d^3\sigma_{incoh}\,\mathcal{I} \tag{3}$$

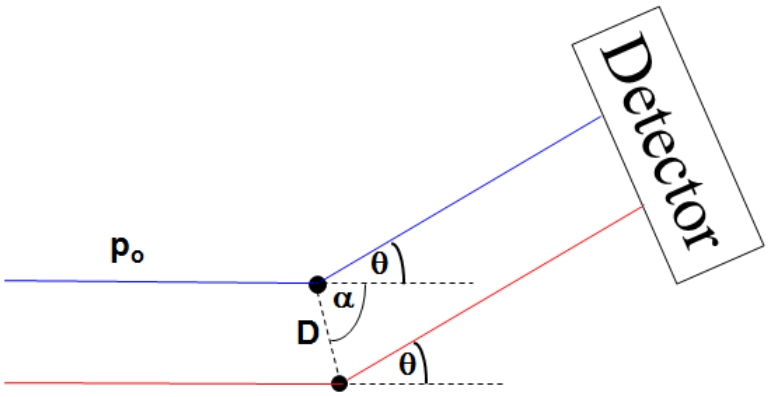

Figure 2.1. Coherent scattering of projectile from identical scattering centers. A projectile proton with de Broglie wavelength $\lambda = h/p_o$ scatters coherently from the nuclei of the H_2 molecule with internuclear separation D. The molecular axis makes an angle α with respect to the initial projectile beam direction.

In the case of a projectile scattering from molecular hydrogen, the triple differential molecular scattering cross-section $d^3\sigma_{H_2}$ represents the coherent cross-section and the incoherent term is approximated as twice the atomic hydrogen cross-section, $2d^3\sigma_H$ [9, 11, 17, 18]. This is reasonable because the atomic system has the same charge and, more importantly, similar ionization potential. The difference between various theoretical models is how the model evaluates the atomic hydrogen cross-section, $d^3\sigma_H$. A major difficulty in modeling single ionization in an ion-atom or ion-molecule collision results from the long range nature of the Coulomb interaction between each of the charged collision partners. For example, in the entrance channel of the collision, the field of the projectile will distort the initial bound state of the target electron. In the exit channel the ejected electron will travel in the combined fields of the scattered projectile and the residual target ion. The scattered projectile also travels in the field of the residual target ion. Additional difficulty arises if the target is a multi-electronic atom or molecule.

Two theoretical models to calculate the triple differential cross-section for single ionization of the hydrogen atom, both based on perturbation theory, will be discussed in this Chapter. First, a modified First Born Approximation (FBA-PCI) will be discussed. This model includes the interaction between the projectile and the target electron in the entrance and exit channels (PCI) of the collision, however it does not include the interaction between the projectile proton and the target nuclei. Second, the continuum distorted wave-eikonal initial state (CDW-EIS) model will be discussed. This model includes all of the physics the FBA-PCI model includes, and in addition includes the interaction between the projectile proton and the target nuclei.

Finally, the derivation of the formal expression for the double differential cross-sections for single ionization of molecular hydrogen, $\frac{d^2\sigma}{d\Omega_{\mathrm{p}}\mathrm{dE_e}}(\theta_p, \Delta\mathrm{E})$, differential in projectile scattering angle and ejected electron energy as a function of the projectile scattering angle θ_{p} and projectile energy loss ΔE for both models, will be outlined. Each of these models provide the basis for theoretical calculations [23] to which the experimental data will be compared in Section 5.3.

2.2. FBA-PCI

In this Section a modified First Born Approximation (FBA-PCI) will be discussed. Consider the scattering of a charged particle by an atomic or molecular target. The event is treated as an effective three-body interaction with the projectile, the (possibly screened) nucleus of the target atom, and the active electron in the collision. The Hamiltonian for the system of particles is given by,

$$H = H_0 + V \tag{4}$$

where $$H_0 = \frac{\boldsymbol{p^2}}{\boldsymbol{2m}} + h_1 \tag{5}$$

Here h_1 is the Hamiltonian for the unperturbed atom or molecule and V is the interaction potential with the projectile. The transition operator T associated with the scattering of the projectile by the atomic center is represented by the Born expansion [24, 25, 26]

$$T=V+VG_0V+VG_0VG_0V+ \ldots \tag{6}$$

where the Green's function, G_0, is defined as,

$$G_0 \equiv \lim_{\varepsilon\to 0}\left(\frac{1}{E-H_0+i\varepsilon}\right) \tag{7}$$

In the first Born approximation the expansion (6) is truncated after the first term.

The case of single ionization of the atomic target by ion impact is treated as an effective three-body process involving the incident projectile with mass M_p and charge Z_p, the ejected electron, and the residual ion with mass M_I and charge Z_T. The triple differential cross-section, differential in the projectile scattering solid angle Ω_p, the ejected electron solid angle, Ω_e and ejected electron energy E_e, can be written in the center-of-mass frame as [27],

$$\frac{d^3\sigma}{d\Omega_{\mathrm{p}}\mathrm{d}\Omega_{\mathrm{e}}\mathrm{dE_e}} = (2\pi)^4 \mu_{Ie}\mu_{pA}^2 \frac{k_f k_e}{k_i} \left|T_{fi}\right|^2 \tag{8}$$

where the reduced masses are given by,

$$\mu_{Ie} = \frac{M_I}{M_I+1} \approx 1, \mu_{pA} = \frac{M_p(M_I+1)}{M_p+M_I+1} \approx \frac{M_I M_p}{M_I+M_p} \tag{9}$$

The momentum vectors of the projectile in the initial and final state $\boldsymbol{k}_i$ and $\boldsymbol{k}_f$ are, respectively [28],

$$\boldsymbol{k}_i = \mu_{pA}\sqrt{\frac{2E_0}{M_p}}, \quad \boldsymbol{k}_f = \mu_{pA}\sqrt{(\frac{2E_0}{M_p})^2 - \frac{2\Delta E}{\mu_{pA}}} \tag{10}$$

where E_0 is the lab-frame energy of the incident projectile, ΔE is the energy loss of the projectile and $\mathbf{k_e}$ is the momentum of the ejected electron. The transition matrix T_{fi} in the FBA is given by,

$$T_{fi} = \left|\langle \Psi_f^{FB} \left| V \right| \Psi_i^{FB} \rangle\right|^2 \tag{11a}$$

with

$$V = \frac{Z_p Z_T}{R} - \frac{Z_p}{|\boldsymbol{R}-\boldsymbol{r}|} \tag{11b}$$

The initial state wave-function $\Psi_{\mathrm{i}}^{\mathrm{FB}}(\boldsymbol{r},\boldsymbol{R}) = (\frac{1}{2\pi})^{3/2}\, e^{i\boldsymbol{k_i}\cdot\boldsymbol{R}}\psi_{1s}(\boldsymbol{r})$ is the product of a plane wave for the incoming projectile and $\psi_{1s}(\boldsymbol{r})$ is the ground state of the atomic

Hamiltonian. Here **R** is the position of the projectile relative to the center-of-mass of the ion-electron system and **r** is the position of the atomic electron relative to the center-of-mass of the ion. In the final state, the projectile is also approximated as a plane wave, $\Psi_f^{FB}(\boldsymbol{R}) = e^{i\boldsymbol{k_f}\cdot\boldsymbol{R}}\psi_f$, where ψ_f is an unperturbed continuum eigenstate with energy $\epsilon = k^2/2$ and quantum numbers (l, m) of the atomic Hamiltonian defined by the partial wave expansion [29],

$$\psi_f(\boldsymbol{r}) = \frac{1}{r\sqrt{k}}\sum_{l,m} i^l\, e^{-i\delta_l} u_{\epsilon l}(r)[Y_l^m(\boldsymbol{r})]^* Y_l^m(\boldsymbol{k}) \tag{12a}$$

where δ_l is the l^{th} partial wave phase shift and $u_{\epsilon l}(r)$ satisfies the asymptotic condition,

$$\lim_{r\to\infty} u_{\epsilon l}(r) = \sqrt{\frac{2}{\pi k}}\sin\left(kr + \frac{1}{k}\ln(2kr) - \frac{l\pi}{2} + \delta_l\right. \tag{12b}$$

The post-collision interaction (PCI) between the ejected electron and the scattered proton is not treated in Eq. (11) because the FBA represents a first order treatment of ionization. On the other hand, PCI can be viewed as a secondary interaction between the scattered projectile and the ejected electron following the ionization of the target. Double [30] and more recently, fully differential cross-sections [31, 32], for the ionization of helium by proton impact have shown that PCI leads to a narrowing of the angular distribution of the ejected electron as the electron is "dragged" by the projectile. In order to account for this PCI in an approximate way Salin [33, 34, 35] found that the FBA cross-section could be multiplied by an overall factor, the Gamow factor, which was originally developed in the

context of nuclear tunneling processes [36]. In the case of single ionization of an atom by ion impact, the Gamow factor depends on the relative electron-projectile velocities. This factor, G_s, is defined as,

$$G_s(\kappa) = \frac{\kappa}{1-\exp(-\kappa)} \tag{13}$$

where $|\boldsymbol{\kappa}| = \frac{2\pi}{\boldsymbol{k_i}/\mu_{pA} - \boldsymbol{k_e}}$. With this factor introduced to include PCI the modified first Born Approximation is termed FBA-PCI.

Applying the above results to Eq. (8) the triple differential cross-section, differential in the projectile scattering solid angle Ω_p, the ejected electron scattering solid angle, Ω_e, and the ejected electron energy E_e, can be written in the FBA-PCI model as,

$$\frac{d^3\sigma}{d\Omega_p d\Omega_e dE_e} = G_s(2\pi)^4 \mu_{Ie} \mu_p^2 \frac{k_f k_e}{k_i} \left|T_{fi}^{FBA}\right|^2 \tag{14}$$

Note that since the initial and final target wave-functions, $\psi_{f,i}$ should be orthogonal, the term Z_pZ_T/R in the potential V, Eq. (14) arising from the interaction of the projectile with the target nucleus (PI), although formally included in the model, does not contribute to the transition amplitude. Therefore, the cross-section, Eq. (16), in the FBA-PCI model, does not include a description of the projectile-target nucleus interaction. In order to account for this interaction a more sophisticated theoretical model is needed. One such model will be discussed in Section 2.3.

2.3. CDW-EIS

Although formally included in the perturbation potential in the modified first Born approximation, as seen in Eq. (14) of Section 2.2 the interaction between the projectile and the target nucleus does not contribute to the scattering amplitude due to the orthogonality between the initial and final electronic states chosen in the model. In order to include this projectile-target nucleus interaction (PI) additional theoretical sophistication is required. One possible theoretical treatment is the continuum distorted wave-eikonal initial state (CDW-EIS) model. In this section, the derivation of the formal expression for the triple differential cross-section $\frac{d^3\sigma}{d\Omega_{\mathrm{p}}\mathrm{d}\Omega_{\mathrm{e}}\mathrm{dE}_{\mathrm{e}}}$, for single ionization of atomic hydrogen by ion impact in this approximation will be briefly outlined and the main features of the model compared, and contrasted with those of the FBA-PCI model.

Like the first Born approximation, the CDW-EIS model is, as far as the operator in the T-matrix is concerned, a first order perturbative method. This means that the transition amplitude is linear in the perturbing potential, V. In addition, the system Hamiltonian remains the same as in Eq. 4. The difference between the FBA-PCI and CDW-EIS models arises in the description of the initial and final states in the transition matrix element, T_{fi}. This effectively accounts for higher order effects such as PI and PCI. The CDW-EIS model was developed by Crothers and McCann [37] as an extension to the CDW approach that was formulated earlier by Chesire [38] to treat capture processes and first applied to the ionization of atoms by Belkié [39]. However, it was found that agreement between CDW results and experimental data was poor, even when compared to the less sophisticated first Born approximation. Crothers determined that the CDW

initial state was not properly normalized, and therefore failed to meet the incoming boundary conditions. The problem was corrected, first in capture processes and later in ionization cross-sections, by replacing the initial distorted projectile state in the CDW wave-function with an eikonal phase factor. In the case of ionization, the eikonal phase depends on the perturbation parameter η, the ratio of the projectile charge to projectile speed. Since the initial development, CDW-EIS has been applied to various collision systems with success, particularly in the scattering plane, in matching the description of the underlying few-body dynamics in ionization processes to experimental results [40, 2, 3].

The CDW-EIS approximation is similar to the FBA-PCI approximation in that the incoming projectile is treated like a plane wave. In the CDW-EIS model, however, PCI is treated by a more sophisticated approach than the Gamow factor utilized in the FBA-PCI model described in Section 2.2. Additionally, the final electronic state is no longer an eigenstate of the target Hamiltonian. As a result, the effect of the PI interaction in the operator of the T-matrix does not vanish as it does in the FBA model. The essential feature of the CDW-EIS model is the inclusion of higher order effects (e.g. projectile-target nucleus interaction and the post-collision interaction between the scattered projectile and the ejected electron) in the final state wave-function and partly in the initial state wave-function. In the entrance channel the initial state is described by a product of the first Born initial state given in Section 2.2 above, and an eikonal phase, $a_i(r, R, \eta) = e^{i\eta \ln\left(\frac{v_p R - \boldsymbol{v_p}\cdot\boldsymbol{R}}{v_p|\boldsymbol{R}-\boldsymbol{r}| - \boldsymbol{v_p}\cdot(\boldsymbol{R}-\boldsymbol{r})}\right)}$, which accounts for the interaction between the projectile and the target nucleus (PI) and the distortion of the initial electronic state due to the field of the projectile [41]:

$$\Psi_{\mathrm{i}}^{\mathrm{EIS}}(\mathbf{r},\mathbf{R},\eta)=\Psi_{i}^{FB}a_{i}(\boldsymbol{r},\eta)=(\frac{1}{2\pi})^{3/2}\,e^{i\boldsymbol{k_i}\cdot\boldsymbol{R}}\psi_{1s}(\mathbf{r})e^{i\eta\ln(\frac{v_pR-\boldsymbol{v_p}\cdot\boldsymbol{R}}{v_p|\boldsymbol{R}-\boldsymbol{r}|-\boldsymbol{v_p}\cdot(\boldsymbol{R}-\boldsymbol{r})})} \qquad (15)$$

where the ratio of the projectile charge to the projectile speed (relative to the target), $\eta=\frac{Z_p}{v_p}$, is the perturbation (Sommerfield) parameter. It should be noted that, since ultimately the interest is in investigating the contribution of the projectile-target nucleus (PI) interaction to the double differential cross-sections as a function of the projectile scattering angle and energy loss, this expression differs from that of Crothers and McCann [37] in that the PI is suppressed in their work. However it is explicitly included in both the entrance channel and the exit channel in the CDW-EIS model used to calculate the theoretical cross-sections of Section 5.3.

In the exit channel, the three charges are moving in their mutual continua. The final state is chosen as a product of the first Born final state, Eq. (12a) in Section 2.3, a Coulomb distortion factor to account for the interaction of the ejected electron with the scattered projectile (PCI) and the interaction of the scattered projectile with the field of the residual target ion. This final state is written as [42],

$$\Psi_{f}^{CDW}(\xi,\boldsymbol{k},\boldsymbol{s})=\Psi_{f}^{FB}N^{*}(\xi)F_{1}^{1}[-i\xi;1;-\boldsymbol{i}ks-i(\boldsymbol{k}\cdot\boldsymbol{s})] \qquad (16)$$

where $\xi=\frac{Z_p}{k}$, **k (s)** is the relative momentum (position) for two-body subsystem, F_1^1 is the confluent hypergeometric function [43], $N(\xi)$ is a normalization factor,

$$N^*(\xi) = \Gamma(1 - i\xi)e^{-\frac{\pi\xi}{2}} \tag{17}$$

and Γ(x) is the gamma function. The transition matrix elements $T_{fi}^{CDW-EIS}$ are defined as,

$$T_{fi}^{CDW-EIS} = \left|\left\langle \Psi_f^{CDW} \middle| V \middle| \Psi_{\mathrm{i}}^{\mathrm{EIS}} \right\rangle\right|^2 \tag{18a}$$

where,

$$V = \frac{Z_p Z_T}{R} - \frac{Z_p}{|\boldsymbol{R}-\boldsymbol{r}|} \tag{18b}$$

The triple differential cross-section for single ionization of an atomic target in this approximation is then [44],

$$\frac{d^3\sigma}{d\Omega_{\mathrm{p}}\mathrm{d}\Omega_{\mathrm{e}}\mathrm{dE}_{\mathrm{e}}} = (2\pi)^4 \mu_{Ie}\mu_p^2\, k_e \frac{k_f}{k_i} \left|T_{fi}^{CDW-EIS}\right|^2 \delta(E_{ef} - E_{ei}) \tag{19}$$

where $E_{ef,i}$ refers to the energy of the electron active in the collision.

Note that like the FBA-PCI model of Section 2.2, the term Z_pZ_T/R in the potential V, Eq. (14b, 20b) arising from the interaction of the projectile with the target nucleus (PI) is also formally included in the model. However, unlike the FBA-PCI model, this potential interaction does contribute to the transition amplitude in the CDW-EIS model. This is because the initial and final target wave-functions, $\psi_{f,i}$ should be non-orthogonal in this model. Therefore, in addition to including the post-collision interaction between the ejected electron and scattered projectile (PCI) the cross-section, Eq. (21), in the

CDW-EIS model, unlike the FBA-PCI model, does include the dynamical effects of the projectile-target nucleus interaction.

2.4. FORMAL EXPRESSION FOR DOUBLE DIFFERENTIAL CROSS-SECTIONS

The FBA-PCI and CDW-EIS expressions for the triple differential cross-sections for ionization of an atomic target described in Sections 2.2 and 2.3 above are not in the desired final form. In order to make a comparison to the present experimental data in Section 5.2, the double differential cross-section $\frac{d^2\sigma}{d\Omega_{\mathrm{p}}\mathrm{dE_e}}(\theta_p, \Delta E)$, differential in the projectile scattering solid angle and ejected electron energy, as a function of the (polar) projectile scattering angle θ_p, projectile energy loss ΔE and averaged over all possible molecular orientations is required. A description of how this obtained from the TDCS of the FBA-PCI and CDW-EIS models will be made in this Section.

Recall from Section 2.1 that, in analogy to the optical Young's double slit experiment, the coherent molecular hydrogen cross-section can reasonably be represented, due the similar ionization potential and like charge, as an incoherent term given by twice the atomic hydrogen cross-section times an interference term [18]:

$$\frac{d^3\sigma_{H_2}}{d\Omega_p d\Omega_e dE_e} = 2\frac{d^3\sigma_H}{d\Omega_p d\Omega_e dE_e}\mathcal{J} \tag{20}$$

The interference term, IT has the form, for *fixed* orientation of the molecule, $\mathcal{J}$=[1 + cos($\boldsymbol{p}_{rec} \cdot \boldsymbol{D}$)] where $\mathbf{p}_{\mathrm{rec}}$= $\mathbf{q}$-$\mathbf{k}_{\mathrm{e}}$ is the momentum of the recoiling residual target ion and

is the difference between $\mathbf{k}_e$, the ejected electron momentum and **q**, the momentum transfer [10, 17, 18]. **D** is the vector directed between the *two* atomic hydrogen centers with equilibrium separation, D=1.4 au

Normally, as in the present experiment, the orientation of the molecule is not measured. Therefore, it is necessary to average the expression for the TDCS, Eq. (22), over all possible orientations of the molecular axis. This can be done analytically [45, 46] and the resulting expression for the TDCS averaged over molecular orientation can be written as,

$$\frac{d^3\sigma_{H_2}}{d\Omega_p d\Omega_e dE_e} = \frac{d^3\sigma_{2H}}{d\Omega_p d\Omega_e dE_e}\left[1 + \frac{\sin(|\boldsymbol{k_e}-\boldsymbol{q}|D)}{|\boldsymbol{k_e}-\boldsymbol{q}|D}\right] \tag{21}$$

It is important to note that Eq. (23) includes the contribution due to the projectile-target nucleus interaction since the momentum transfer **q** appears explicitly in the interference term. This is particularly critical because the distribution of the transverse component of **q** (i.e. in the direction of the initial projectile beam axis), $\boldsymbol{q}_\perp = \mathbf{p}_0 \sin\theta_p$**,** where $\mathbf{p_o}$ is the initial projectile momentum and θ_p is the polar projectile scattering angle, is measured in the present experiment. Since D=constant in Eq (23) and for the kinematic boundary conditions studied in this work, $\mathbf{k_e}<\mathbf{q}$, the interference term depends most strongly on **q**. However, any other possible contribution to the interference due to the electron emission spectra is included in the molecular cross-section as well.

In the present experiment, double differential cross-sections differential in the projectile solid angle Ω_p and the ejected electron energy E_e, are needed, so that an integration of Eq. (23) over the electron emission spectra (or equivalently the recoil-ion

momentum) is required. The expression for the double differential cross-sections $\frac{d^2\sigma_{H_2}}{d\Omega_p dE_e}$ can then be written as [47],

$$\frac{d^2\sigma_{H_2}}{d\Omega_p dE_e} = \sqrt{2E_e}\int \frac{2d^3\sigma_H}{d\Omega_p d\mathrm{E_e} d\Omega_\mathrm{e}}\left[1+\frac{\sin(|\boldsymbol{k_e}-\boldsymbol{q}|D)}{|\boldsymbol{k_e}-\boldsymbol{q}|D}\right]\mathrm{d}\Omega_\mathrm{e} \qquad (22)$$

For the two models, FBA-PCI and CDW-EIS, discussed in Sections 2.2 and 2.3 respectively, the relevant atomic cross-section is substituted into Eq. (24). As discussed in Section 5.3, in comparing theoretical results to the present experimental data, by taking the ratio of the experimental data to twice the atomic cross-section for each model the explicit contribution to the interference term due to the inclusion of the projectile-target nucleus (also called the N-N interaction) can be investigated further.

3. EXPERIMENTAL SETUP

3.1. OVERVIEW

In this chapter, a description of the experimental setup is presented. The experiment was performed at the Missouri University of Science and Technology 3-body momentum spectrometer. The overall experimental set-up is shown schematically in Figure 3.1. A 5 keV proton beam with an energy spread of less than 1 eV was generated from a hot cathode ion source, accelerated to 75 keV, and collimated by a set of slits 0.1 mm by 0.1 mm in size. The protons crossed a cold neutral molecular hydrogen target beam from a supersonic jet. The recoil ions were extracted from the interaction region by a weak electric field and arrived on a position sensitive detector. The scattered proton beam was decelerated by 70 keV and energy analyzed by an electrostatic parallel plate analyzer. The projectiles were then detected by a position sensitive detector where the projectile scattering angle was determined from the position on the detector. The projectile and recoil-ion detectors were set in coincidence. In the following sections each of the various components of the experiment are described in detail.

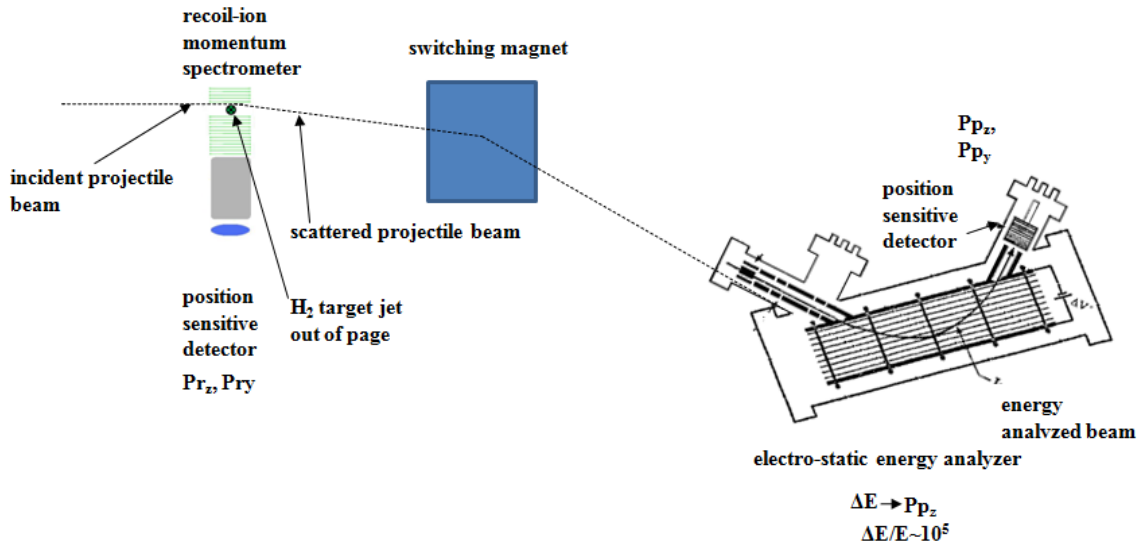

Figure 3.1. Overview of experimental set-up. Recoil ions and scattered projectile protons are detected in coincidence (see Sections 3.7 and 4.2).

3.2. HOT CATHODE ION SOURCE AND ACCELERATOR

The projectile protons are generated in a hot cathode ion source. An exploded view of the ion source is shown in Figure 3.2 [48]. Primary electrons are produced by a thoriated tungsten filament and are accelerated by a low voltage (approximately 80 V) towards the anode. The filament supply typically operates at 12 V and 15 A. These primary electrons ionize and dissociate the hydrogen molecules of the source gas, thereby creating secondary electrons. A 3:1 mixture of argon to hydrogen is used to increase the production of secondary electrons. Eventually this process leads to a sufficient number of ions and electrons being created, such that a self-sustaining discharge (plasma) is obtained.

This source is known to produce ion beams with an energy spread of much less than 1 eV [49] and proton currents of >30 nA are realized during operation. The lifetime of the filament is approximately 100 hrs and is primarily limited by ion impact on the

filament by ions created in the source. The bias of the source is such that ions are accelerated towards the filament and away from the extraction aperture. This is commonly referred to as "reverse biasing" the source, since the direction of the ion trajectories is opposite the direction required for maximum extraction efficiency. This reverse bias allows only ions created very near the extraction aperture to exit the source. This reduces the overall energy spread by minimizing variations in the plasma potential. Ions exiting the source anode are accelerated to 5 keV.

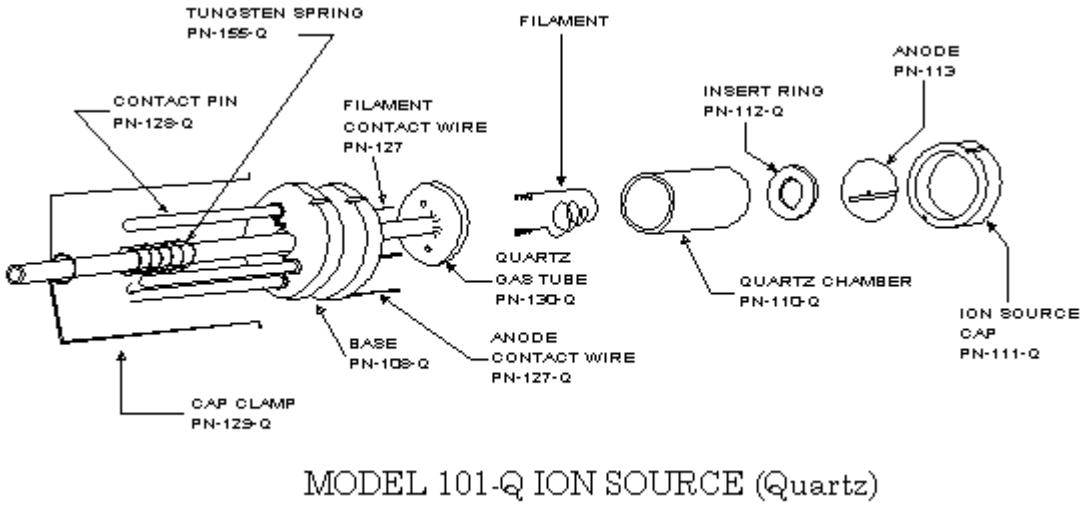

Figure 3.2. Hot cathode ion source [45].

Ions created in the source include H^+, H_2^+, and multiple charge states of argon. A Wien filter is used to separate these ions by charge state and mass, sweeping all but the desired protons from the beam. In a Wien filter [50], a constant electric field $\vec{E}$ and magnetic field $\vec{B}$ are crossed such that the magnetic force on a charged particle moving with speed v in this field is pointing exactly opposite to the electric force. The force on a

charged particle traveling with speed v/c<<1 is governed by the classical Lorentz force Law:

$$\vec{F} = q(\vec{E} + \vec{v} \times \vec{B}) \tag{25}$$

For a given combination of $\vec{E}$ and $\vec{B}$ there is a specific ratio of charge to mass q/m for which the net force acting on the particle is zero:

$$qE = qvB \tag{26a}$$

$$\therefore E = vB \tag{26b}$$

The kinetic energy of the proton beam after extraction from the source by potential difference $U_{extraction}$ is given by,

$$\frac{1}{2}mv^2 = qU_{extraction} \tag{27}$$

Combining Eqs. (26) and (27),

$$E^2 = \frac{2qU_{extraction}}{m} B^2 \tag{28}$$

If E and B are chosen so that the net force is zero for q/m=1 then protons are not deflected from the beam. No other beam component has the same q/m so the proton beam is cleaned of the other charge/mass states produced in the hot cathode source.

These protons are then further accelerated to an energy of 75 keV and the beam direction is controlled by four sets of electric deflectors through a pair of slits such that the beam is collimated to 0.01 mm^2. The beam is then guided through the target region.

3.3. TARGET BEAM PRODUCTION

The energy transferred to the recoil-ion in an ionizing collision is typically very small, only a few meV. However, the thermal energy spread at room temperature is approximately 30 meV. In light of this, the target temperature must be reduced or it would be impossible to measure the recoil-ion momentum with sufficient resolution to provide a sensitive test of theoretical models. Although the double differential cross-sections measured in this work do not require knowledge of the recoil-ion momentum, the experimental set-up was designed with the ultimate goal of measuring fully differential cross-sections for atomic and molecular hydrogen simultaneously by measuring the momentum of the scattered projectiles and recoil ions in coincidence. Therefore, the full capabilities of the experimental set-up are described.

Supersonic jets have been in extensive use in atomic and molecular physics experiments for more than 50 years [51]. The fundamental principle behind the production of a supersonic jet is an adiabatic expansion in the desired jet direction. Consider a nozzle of diameter d connected to a gas reservoir in which there is a backing pressure P_o. For pressure ratios between the outside of the walls of the aperture and the reservoir larger than approximately two [52] gas pushed through a small aperture into a reservoir at low pressure is accelerated to supersonic speed at the exit of the aperture. The result is adiabatic cooling of the gas in the direction of the pressure gradient. A

supersonic jet which extends well over 10 cm beyond the nozzle can be obtained for the condition $P_o d > 1 \text{torr} \cdot \text{cm}$ [52]. The momentum of the gas in the direction of the jet is given by $P_{jet} = \sqrt{5\, k_b T_o M}$, where M is the mass of the target gas, k_b is the Boltzmann constant, and T_o is the initial temperature of the gas in the reservoir, typically 300 K. Additionally, by "skimming" the fastest part of the gas at a point just beyond where the speed of the gas becomes supersonic (the so-called zone of silence) a jet with greatly reduced momentum spread in the direction perpendicular to the jet axis can be achieved. With aluminum or stainless steel machining techniques an aerodynamic skimmer can be created that does this with tremendous efficiency. If $P_o d < 1 \text{Torr} \cdot \text{cm}$, a target jet may still be obtained, however the nozzle-to-skimmer distance becomes a critical parameter as the region of supersonic flow will only extend behind the nozzle a few nozzle diameters. In most cases, P_o is approximately 2-3 atm so that $P_o d < 1 \text{Torr} \cdot \text{cm}$ is satisfied for nozzle diameters as small as 10 μm. P_o is mainly limited by the pressure outside of the skimmer, which in turn depends on the pumping speed of the vacuum system for the particular target species.

As mentioned above, the apparatus was designed with the ultimate goal of obtaining fully differential cross-sections for atomic and molecular hydrogen simultaneously. For an atomic hydrogen target, there are special requirements that significantly complicate the experimental set-up compared to, for example, a helium target [30, 31]. In order to produce an atomic hydrogen target beam, dissociation of the molecule is required. One condition that arises from this fact is that the microwave discharge used for production of atomic hydrogen requires an operating pressure of $P < 1$ Torr. This results in a much smaller pressure gradient than can be accomplished with

other targets, e.g. helium, using a conventional jet, and therefore less adiabatic cooling in the direction of the target gas. Subsequently, the target jet density is also much lower than, for example, a helium jet operating at a much higher pressure as described above. In order to compensate for the requirements imposed by dissociation, a special design for the target jet assembly with regard to location and material was necessary. Additionally, some modifications to the recoil-ion momentum spectrometer were required (see Section3.6).

The target jet assembly is illustrated in Figure 3.3. Hydrogen gas was pushed through a nozzle formed from a Teflon coated quartz capillary, diameter approximately 0.8 mm, which is attached to the gas reservoir manifold via 6.35 mm diameter Teflon tubing. Teflon is required when production of H atoms is desired, as the recombination rate of H is low on Teflon [53]. The backing pressure in the tubing was 500 mtorr as measured by a thermo-couple gauge at the inlet and the pressure around the capillary was maintained at 10^{-3}- 10^{-4} torr by a 400 l/s turbo-molecular pump. A Teflon skimmer (diameter ~0.3 mm) was placed between the nozzle and the target chamber. The skimmer was constructed of Teflon due to its location inside the recoil-ion momentum spectrometer (see Section 3.4).

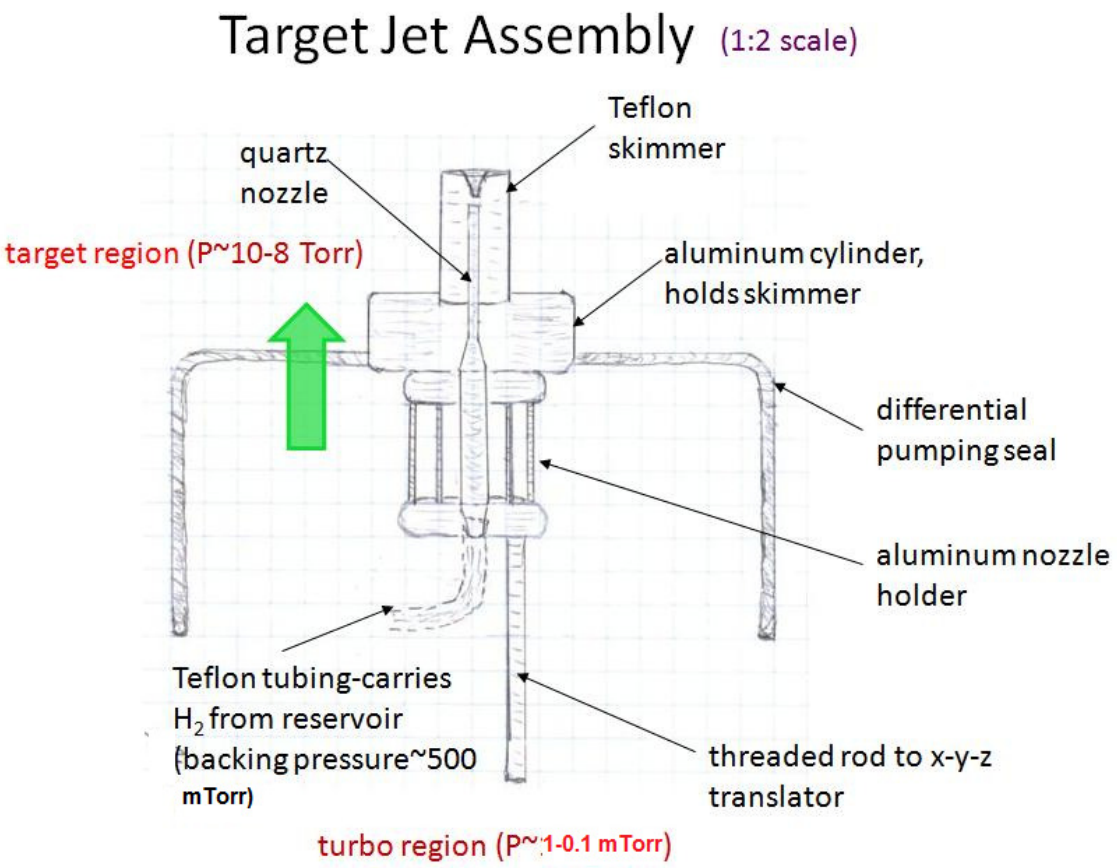

Figure 3.3. Target jet production. Teflon tubing supplies gas to target region via the quartz nozzle. A large pressure gradient (indicated by green arrow in figure) results in an adiabatic expansion and therefore cooling along the target jet axis. The Teflon skimmer removes the fastest component of the beam parallel to the target jet axis.

The pressure in the target chamber was approximately 10^{-7} torr with the full target gas load. The skimmer-to-nozzle distance was chosen to ensure the jet was cut out of region behind the nozzle where supersonic flow was maintained. As discussed above, the skimmer removed the fastest component of the gas jet perpendicular to the projectile beam axis and provided collimation. The result was a cold, well-collimated target gas jet.

3.4. RECOIL-ION MOMENTUM SPECTROMETER

The recoiling molecular hydrogen ion is extracted from the target region by a weak electric field by the recoil-ion momentum spectrometer, represented schematically in Figure 3.4. The spectrometer is a modification of the basic Wiley-McLaren type [54] and consists of electric plates separated by nylon spacers and electrically connected to each other via a resistor chain. As mentioned in Section 3.3, the spectrometer was designed ultimately for use in a kinematically complete experiment with an atomic hydrogen target. The intersection of the target and projectile was located approximately in the middle of the spectrometer between two extraction plates. The plates are connected via a resistor chain in order to create a homogeneous electric field of approximately 3 V/cm.

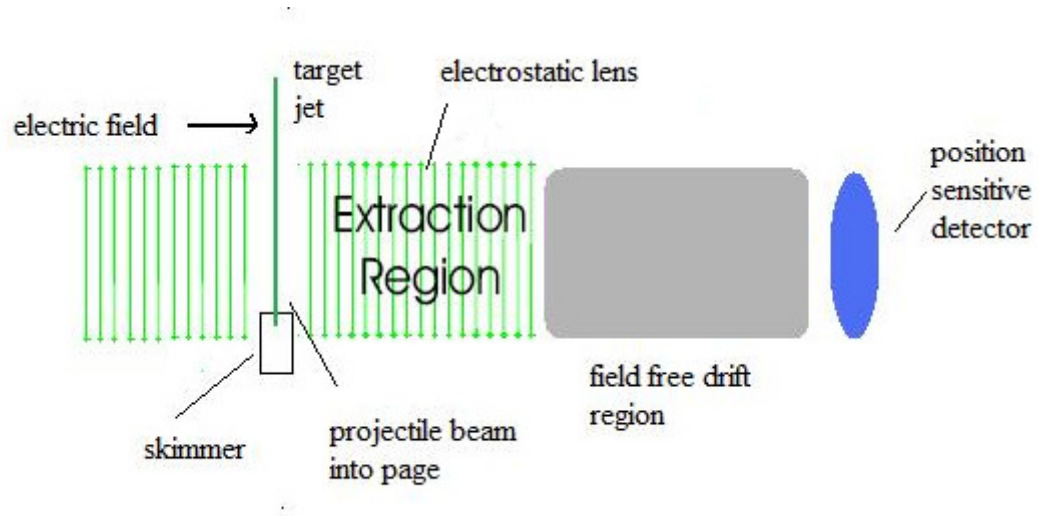

Figure 3.4. Recoil-ion momentum spectrometer. The drift region is twice the length of the electric field region for time focusing. The electrostatic lens provides spatial focusing.

After the acceleration region, the recoil-ions enter a drift tube that is 20cm in length. The drift region is twice the length of the acceleration region, which allows for time focusing such that ions that spend different times in the acceleration region due to their different starting positions arrive at the detector at the same time [55]. The introduction of an electrostatic lens, as indicated in Figure 3.4, provides spatial focusing such that ions that are created at different positions along the spectrometer axis arrive at a single spot on the detector, however the displacement on the detector in the x- and y-directions is still proportional to the components of the recoil-ion momentum in those directions. The third component of the recoil-ion momentum is given by the coincidence time spectrum (see Figure 4.1, Section 4.2). Although the projectile beam and the target jet are well collimated the finite extent of the target volume, the overlap of the target beam and the projectile beam, contributes to the spread in the recoil-ion momentum distribution, i.e. to the momentum resolution. However, in the direction of the extraction field this component of the recoil momentum resolution is essentially eliminated by the time focusing. The use of the electrostatic lens partially accounts for this spread along the direction of the projectile beam and both the time and spatial focusing improve the momentum resolution capabilities of the spectrometer.

As discussed in Section 3.3, the low backing pressure required for operation of the microwave discharge results in a target jet that has both a reduced density and smaller spatial extent into the target region when compared to e.g. a helium jet with 2-3 atm of backing pressure. Therefore, the jet assembly was located partially inside of the recoil-ion momentum spectrometer to put it as close as possible to the projectile beam. As a result, the skimmer was constructed of Teflon to avoid distortion of the electric field

inside the spectrometer. The use of Teflon instead of metal limits the machining techniques available to produce a aerodynamically optimized skimmer shape. Therefore, for a fully differential measurement the recoil momentum resolution in principle could be compromised. In addition, if the projectile beam comes close enough to the skimmer, charging of the skimmer could occur. However, the distance of the skimmer from the projectile beam was sufficiently large to prevent charging of the skimmer by the beam. This was clearly indicated by the stability of both the projectile beam and the extracted recoil-ion beam. Since the recoil-ion momentum is not needed for the double differential cross-sections of interest in this work, the problems with recoil-ion momentum resolution discussed above are of no direct concern for the present work. However, initial measurements of the recoil-ion momentum distribution clearly show surprisingly good momentum resolution in both directions as well as excellent separation of the ionization and capture lines (see Figure 3.5). This also demonstrates that the charging of the Teflon skimmer was not a restriction.

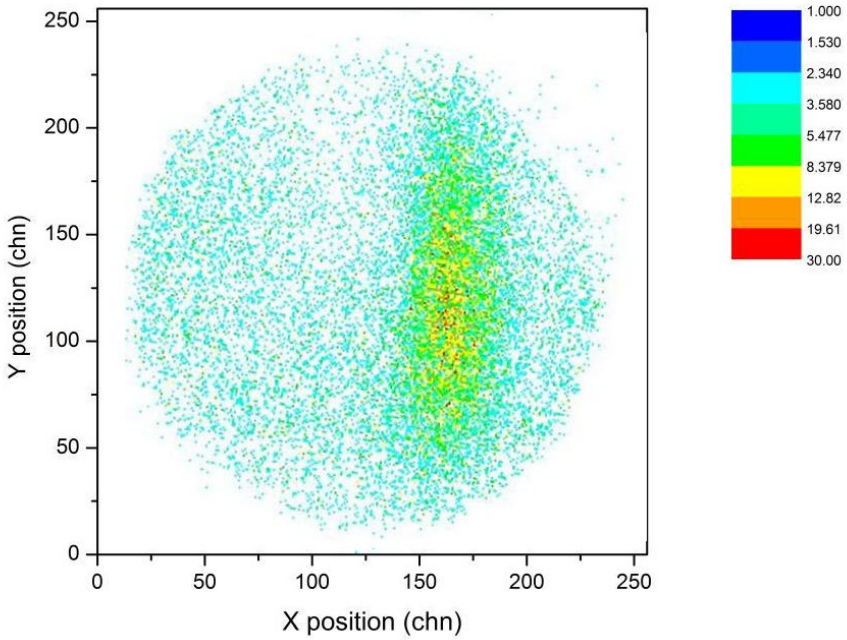

Figure 3.5. Sample image of recoil-ion distribution taken with microwave discharge on. The momentum resolution is estimated to be <0.2 au

3.5. POSITION SENSITIVE MULTI-CHANNEL PLATE DETECTOR

The recoil-ion momentum spectrometer (see section 3.4 above) and the projectile momentum analyzer (see section 3.6 below) both utilize position sensitive multi-channel plate (MCP) detectors. The detectors in this experiment utilize the chevron geometry as pictured in Figure 3.6. In this geometry, two multi-channel plates are stacked on top of each other. Each multi-channel plate is made from a stack of millions of individual electron multiplier tubes. Each tube has a diameter of typically 10 μm and a length of about 1 mm. Typically the active area of the detector is 50% of the total area. The front and back surface of an MCP is coated with metal to form input and output electrodes, however the inside of the tubes is covered with a semi-conducting layer that emits

secondary electrons under the impact of primary energetic particles, such as UV photons or charged particles such as ions or electrons. By biasing the MCP electrodes with a high electric field (approximately 1000V/mm), each of the secondary electrons gains enough kinetic energy to free more electrons when it hits the wall of a channel. An avalanche of electrons is formed along the tube that has a charge of a few thousands to a million e, depending on the ratio of the length of the tube and the diameter, and the electric field. A large charged cloud is centered at the location of impact of the primary particle. Thus, an MCP can be used for photon and particle imaging. In order to determine the position of the primary particle, the detectors used in this experiment utilize a wedge and strip anode at the back side of the detector [56]. The amplified electron cloud exiting the MCP is accelerated onto a segmented anode that has electrically separated areas with a wedge and strip structure as pictured in Figure 3.6. The area of the wedges (green) and strips (red) depends linearly on the x- and y- position, so the pulse heights of the signals picked up at both electrodes are proportional to the position of the centroid of the electron cloud.

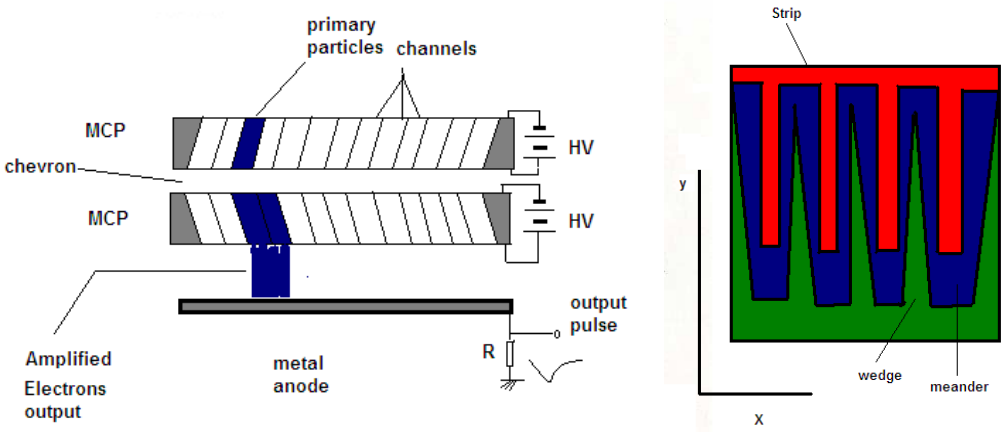

Figure 3.6 Principle of operation of channel plate detector. Structure of a wedge and strip anode with an extremely reduced number of periods showing x- and y- dependence.

The pulse heights of the wedge and strip are normalized to the total collected charge, which is the pulse-height sums of the wedge, the strip, and the filler between the two, called the meander (blue). The signals from all three electrodes are amplified by individual fast charge sensitive preamplifiers and amplifiers and the output recorded by analog-to-digital converters. The normalization and calibration for each event is done by computer software and a small sample of the pulse height distributions is examined on the computer during data taking to verify correct operation. The position information is obtained from the measured pulse heights which depends on the amount of charge collected by the wedges Q_W, the stripes Q_S, and the meander Q_M,

$$X \propto \frac{Q_S}{Q_S + Q_W + Q_M}, Y \propto \frac{Q_W}{Q_S + Q_W + Q_M} \tag{29}$$

For coincidence experiments, a timing signal can be picked up at either the front or back of the MCP stack. Position resolution of ±50 μm (0.1 mm FWHM) and time resolution of <1ns is obtainable with typical detectors in this geometry [57].

3.6. PROJECTILE MOMENTUM ANALYZER

After exiting the target chamber, the projectile beam continues through a switching magnet where neutralized projectiles are swept out of the beam. The projectile momentum is measured in polar coordinates. The magnitude of the projectile momentum is determined from energy analysis and the direction is determined from position-sensitive detection.

The energy of the scattered projectile protons is measured by a 45º parallel plate electrostatic analyzer. The required energy resolution is approximately 5 eV. The theoretical resolution of the analyzer is given by

$$\delta E = E\frac{2w}{l} \tag{30}$$

where w is the width of the analyzer slits and l is the distance between the entrance and exit slits of the analyzer. For E=75 keV and w=0.075 mm the required distance between the entrance and exit slits would be approximately 5 m. Clearly this is not feasible. In order to reduce the required length of the analyzer the projectiles are decelerated to 5kV prior to energy analysis. The actual distance between the analyzer slits is 0.35 m, giving a theoretical absolute energy resolution of 2 eV for 5keV projectiles. This is consistent with the measured resolution (3 eV FWHM) [49].

The 45º electrostatic parallel plate energy analyzer is shown schematically in Figure 3.7.

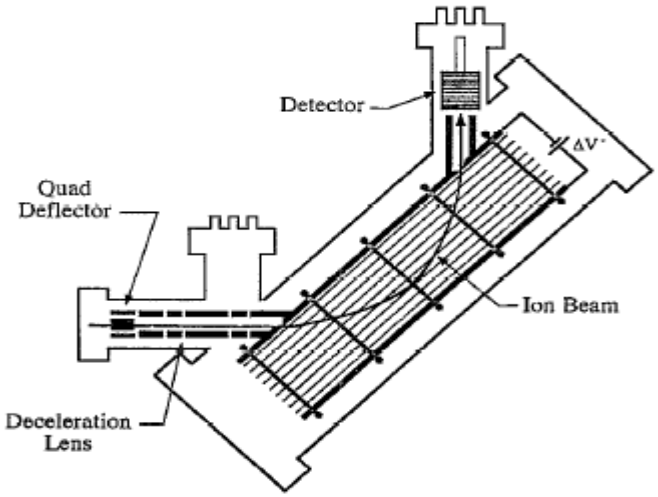

Figure 3.7. Projectile Momentum Analyzer

The energy of the scattered proton projectiles is determined by the difference between the acceleration and deceleration potentials, by the extraction voltage at the ion source, and by the energy lost in the collision with the target molecule. The acceleration and deceleration terminals are fed by a single high voltage supply to cancel any fluctuations in this voltage. The decelerator is held at 70 kV. An offset voltage ΔV, relative to the decelerator ground is added to the decelerator potential. The output of this offset voltage supply is then connected to the accelerator terminal so that the total potential of the accelerator terminal relative to ground is V_{acc} is $V_{dec}+\Delta V$. Prior to the collision projectile protons have an energy $E_i=q(V_{dec}+V_{ex}+\Delta V)$, where q is the charge of the projectile and V_{ex} is the ion source extraction voltage, 5 kV. After the collision the projectiles have an energy, $E_f=q(V_{dec}+V_{ex}+\Delta V)-\Delta E$, where ΔE is the energy lost by the projectile in the collision. After deceleration, and upon entering the electrostatic energy analyzer, the projectile energy is,

$$E_{dec}=q(V_{dec}+\Delta V+V_{ex})-\Delta E-qV_{dec}=qV_{ex}+q\Delta V-\Delta E \quad (31)$$

If $q\Delta V=\Delta E$ then $E_{dec}=V_{ex}$. Therefore, the energy analyzer is set to a constant pass energy of qV_{ex}=5keV so that only projectiles which lost an energy equal to $q\Delta V$ in the collision are detected. The energy-loss spectrum can be obtained by scanning ΔV. A typical energy loss spectrum, for fixed zero scattering angle, with the counts plotted as a function of the energy lost by the projectile in collision is shown in Figure 3.8 [58].

After being energy analyzed the projectiles are detected by a position-sensitive multi-channel plate detector (see Section 3.5 above) in coincidence with the recoil ions.

The entrance and exit slits of the energy analyzer are long in the x-direction, approximately 2 cm, and extremely narrow in the y-direction, approximately 75 μm, so that the azimuthal scattering angle of the detected projectiles is fixed to 0° and the polar scattering angle θ_p is given by the position information of the detector. The projectiles were detected with an absolute energy resolution of ±1.5 eV and an angular resolution of ±50 μrad. The projectile energy loss, ΔE, is equal to the ejected electron energy E_e plus the ionization potential of the H_2 molecule, 15.4 eV. As will be discussed further in Section 4.2., the coincident projectile position spectrum for a fixed energy loss is directly proportional to the double differential cross-sections, as a function of the projectile polar scattering angle.

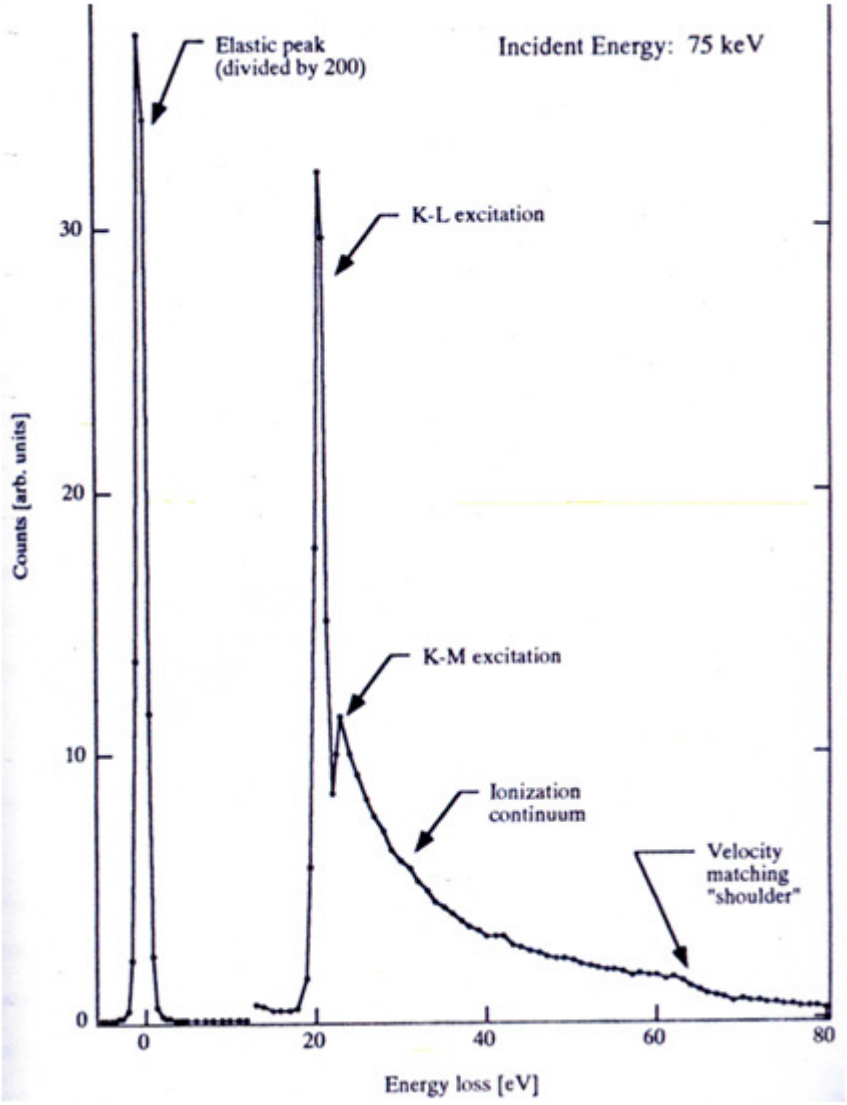

Figure 3.8. Typical Projectile Energy Loss Spectrum. Counts (arbitrary units) are plotted as a function of energy lost by the projectile in the collision for a fixed scattering angle of 0°, in this instance for 75 keV proton impact on helium [58]

3.7. DATA COLLECTION ELECTRONICS

Figure 3.9 is a block diagram of the electronics used to collect the coincidence projectile spectrum in this experiment. The wedge, stripe, and meander signals (see Section 3.4 above) from the projectile detector were amplified by charge sensitive

preamps and amplifiers. The timing signal was amplified by a fast timing amplifier. In order for the signals from the projectile detector, which was located inside the decelerator terminal at high voltage, to reach ground, the amplified signals were converted to optical signals via a fiber optic transmitter and transmitted over fiber-optic cable where a receiver converted the signals back to analog electrical pulses [59].

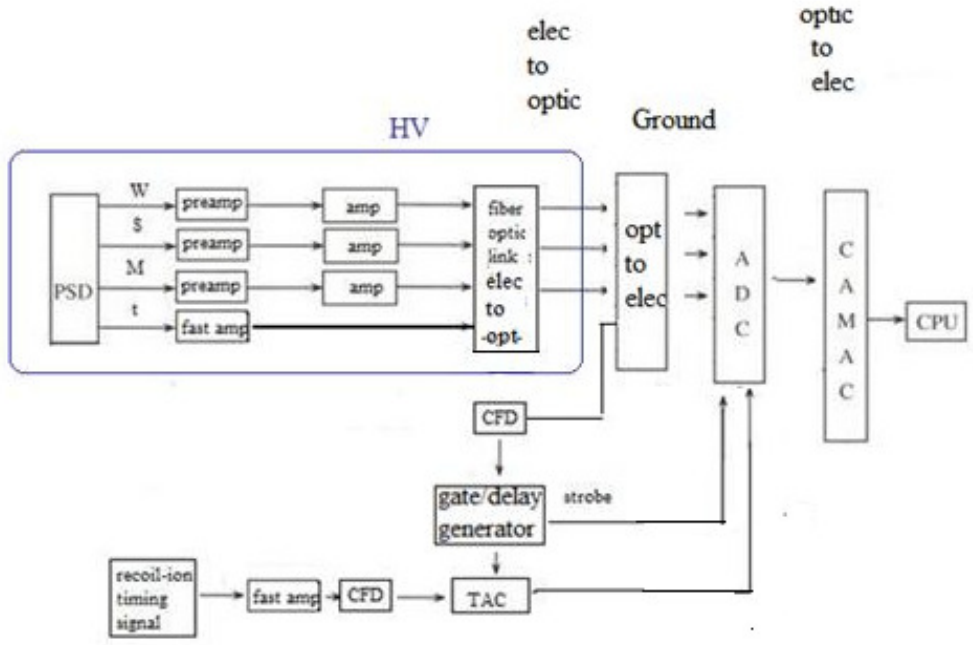

Figure 3.9. Block diagram of data collection electronics. The abbreviations used are PSD: Position Sensitive Detector, W: Wedge, S: Stripe, M: Meander, t: projectile timing signal, ADC: Analog-to-digital converter, CFD: Constant Fraction Discriminator, TAC: Time-to-Amplitude Converter, CAMAC: Computer Automated Measurement and Control.

The wedge, stripe, and meander signals were converted to digital pulse by an analog-to-digital converter. These digital pulses were sent to a computer for data collection over a standard GPIB connection. The fast timing signals picked up from the back of the projectile and recoil-ion detectors were amplified and shaped by fast preamplifiers and then sent to constant fraction discriminators (CFD).

The primary purpose of the CFD is to eliminate electronic noise from the detector and amplifier [60]. Timing signals from the detector may vary in amplitude from event to event, however the rise time (or shape) of the pulse is constant from event to event. The variation in amplitude of the timing pulse can lead to timing errors [61]. The constant fraction discriminator ensures that the timing signal is independent of amplitude. This is done in the CFD by dividing the input signal into two signals. One signal is delayed and inverted while the amplitude of the other signal is attenuated by a constant fraction. When the amplitude of the delayed, inverted input reaches the constant fraction of the input amplitude, the combined signal reaches a zero crossing. The zero crossing occurs at the time when the inverted and delayed input signal has risen to this constant fraction of its maximum amplitude. This point is detected by a fast comparator inside the CFD and a corresponding timing output pulse is generated.

The timing signals generated from the projectile and recoil-ion detectors, respectively, are then combined in a time-to-amplitude converter (TAC) to generate a coincidence time spectrum. The recoil-ion timing signal is used as the start for the TAC and the delayed projectile signal as the stop signal, which ensures that the stop signal always arrives at the TAC after the start signal. A time window is set in the TAC controls, which is typically approximately 10μs. Events corresponding to the detection of a recoil-ion and scattered projectile proton that have a difference in time-of-detection that falls within this time window are called coincident events and are passed to the ADC. Events that do not fall within this time window are rejected. The amplitude of the output signal of the TAC is directly proportional to the time difference between the start and the

stop signal [62]. The TAC signal was then sent to the ADC and finally to the data collection computer.

A strobe signal gate triggered by the projectile timing signal is used to initiate a conversion cycle in the ADC. The data registers of the ADC were controlled and output by the Computer Automated Measurement and Control (CAMAC) data bus via a computer interface and managed by data collection software for storage on a computer. As described in Section 3.5, the three position signals, W, S, and M, from the projectile detector are used in the software to generate event by event position spectrum of projectiles arriving on the detector. The timing information from the TAC is used in the same software to generate a time difference spectrum [63]. The use of these two spectra in generating normalized doubly differential cross-sections will be described in Chapter 4.

4. DATA ANALYSIS

4.1. OVERVIEW

In this chapter, the procedure for converting the raw position and time signals from the projectile and recoil-ion detectors, to normalized doubly-differential cross-sections $d^2\sigma/d\Omega_p dE_e\,(\theta, \Delta E)$, where Ω_p is the projectile solid angle, and E_e is the ejected electron energy, will be discussed. This conversion can be categorized into three major steps. First, the coincidence time spectrum between the projectiles and recoil ions was used to select $p+H_2$ ionization events that were correlated in time, i.e. events in which the detected projectile and the detected recoil ion originated from the same collision. Random coincidences are events in which the detected projectile and detected recoil ion *did not* originate from the same collision, and therefore do not result in a well-defined time difference between the detection of both particles. Events in the 2-D projectile spectrum corresponding to the flat background in the time spectrum, due to random coincidences, were subtracted from events corresponding to the time peak, the correlated (true) coincidences, in the raw 2-D projectile spectrum. In a third step, this "clean" 2-D projectile position spectrum was calibrated (i.e. converted from channel number to a relative scattering angle in mrad) using a conversion factor obtained from the calibration procedures described below. This distribution was then normalized to the total ionization cross-section [64], obtaining the normalized DDCS.

4.2. ANALYSIS OF COINCIDENCE TIME SPECTRUM

Figure 4.1 shows a typical coincidence time spectrum, as discussed in Section 3.7. In this case the time spectrum is presented as a function of channel number. The peak in the coincidence spectrum centered near channel number 173 reflects the time-of-flight difference between the projectile protons and the H_2^+ recoil ions.

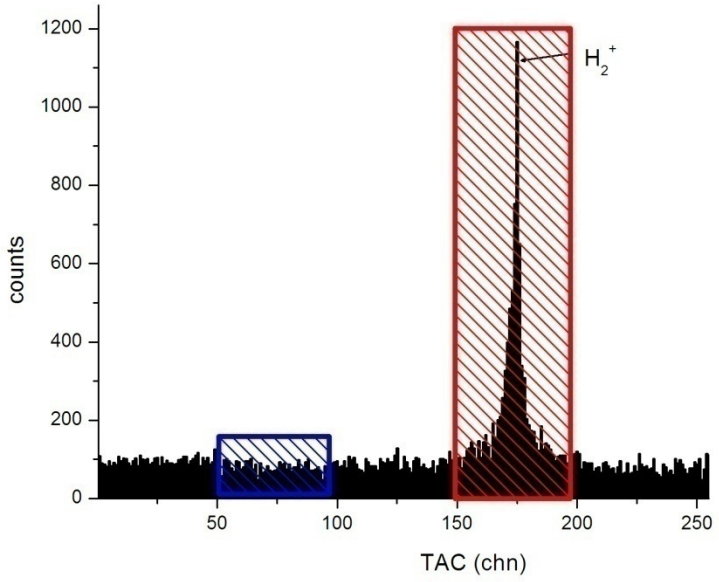

Figure 4.1. Sample TAC Spectrum. The red hashed region represents the gate on the centroid of the time peak and the blue hashed region of the same width are used to set acondition on the 2-D projectile spectrum for random subtraction.

In principle the recoil-ion momentum distribution along the spectrometer axis is reflected in the shape of the time peak, however for the doubly-differential cross-sections of interest here, only the time difference is important. The primary purpose of the coincidence spectrum is to select valid p+H_2 ionization events using this time peak. In a coincidence experiment, as briefly noted in Section 3.7 and Section 4.1 above, there are

two types of coincidence events: (a) events corresponding to the detection of a scattered projectile proton and a detected recoil-ion resulting from the same collision event, which are called "true" coincidences and have a definite time correlation, and (b) events corresponding to the detection of a projectile proton and a detected recoil ion that were not from the same collision, "random" coincidences, and therefore do not have a definite time correlation. Only the peak in the time spectrum, labeled H_2^+, in Figure 4.1 contains true coincidences. However, the area under this time peak, as well as the rest of the coincidence time spectrum, also contains random coincidences and therefore there are data in the 2-D projectile position spectrum which correspond to these random coincidences. The time peak in this experiment was used to select valid $p+H_2$ ionization events in the 2-D projectile position spectrum from which the flat background due to random coincidences is subtracted to remove the events corresponding to random coincidences (random subtraction).

Random subtraction is accomplished by setting a gate centered on the centroid of the time peak, depicted as the red hashed region in Figure 4.1, and setting a gate of the same width on a region not included in the time peak, depicted as the blue hashed region in Figure 4.1. These two regions are used to set a condition on the 2-D projectile spectrum, generating one 2-D spectrum, Figure 4.2 (a), corresponding to both the true coincidences and the random coincidences under the envelope of the time peak and another 2-D projectile position spectrum representing only the random coincidences. These two spectra are then subtracted, resulting in a "clean" 2-D projectile spectrum corresponding to only true coincidences, Figure 4.2 (b). The image of the energy analyzer

slit, discussed in Section 3.5, can also be clearly seen in these spectra. The “clean” 2-D projectile position spectrum was then ready to be converted to an angular distribution.

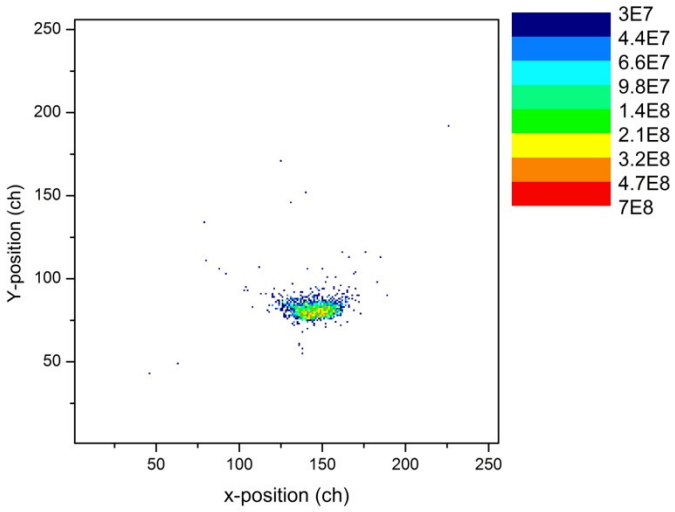

(a)

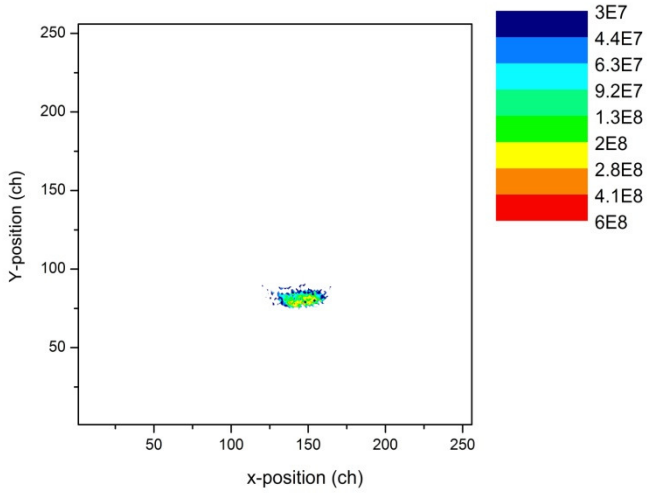

(b)

Figure 4.2. Projectile position spectrum before (a) and after (b) random subtraction

4.3. ANGULAR CALIBRATION

The displacement of the projectile on the detector in the x- direction is directly proportional to the polar scattering angle. The projection, along the x-axis, of the 2-D spectrum in Figure 4.2(b) gives this distribution. In order to determine the scale factor, which transforms the linear displacement to an angular one, a calibration is needed. The scale factor was determined by two independent methods. The first method of determining the scale factor involved collecting data for a helium target at a projectile energy loss of 30 eV. This data was fit to the previous results for the same kinematic conditions [30]. In that experiment, Schulz et al. did not use a position-sensitive detector as in the present experiment. Instead, the accelerator was rotated around the target region by an accurately known angle using a high precision stepping motor system. From a fit of the present helium data to those of Schulz et al, it was determined that the angular acceptance of the entire position-sensitive projectile detector is approximately 4.45 mrad.

In order to verify the calibration described above, a second, geometric method was employed. For projectiles with line of sight to the detector, the angular acceptance would simply be the ratio of the active width of the detector to the total straight-line path length. However, in this experiment the geometry is complicated by the deceleration of the scattered projectiles and the parabolic motion through the energy analyzer. The values of quantities important to the calculation are summarized in Table 4.1 and indicated schematically in Figure 4.3.

Quantity	Description of measurement	Value
d	target chamber to deceleration column	2290 mm
a	deceleration column	710 mm
b	deceleration column to analyzer front slit	380 mm
l	width of energy analyzer	123 mm
R	entrance to exit slit	356 mm
c	exit slit to detector	300 mm
s	path length in analyzer	447 mm

Table 4.1. Distances related to geometric calibration.

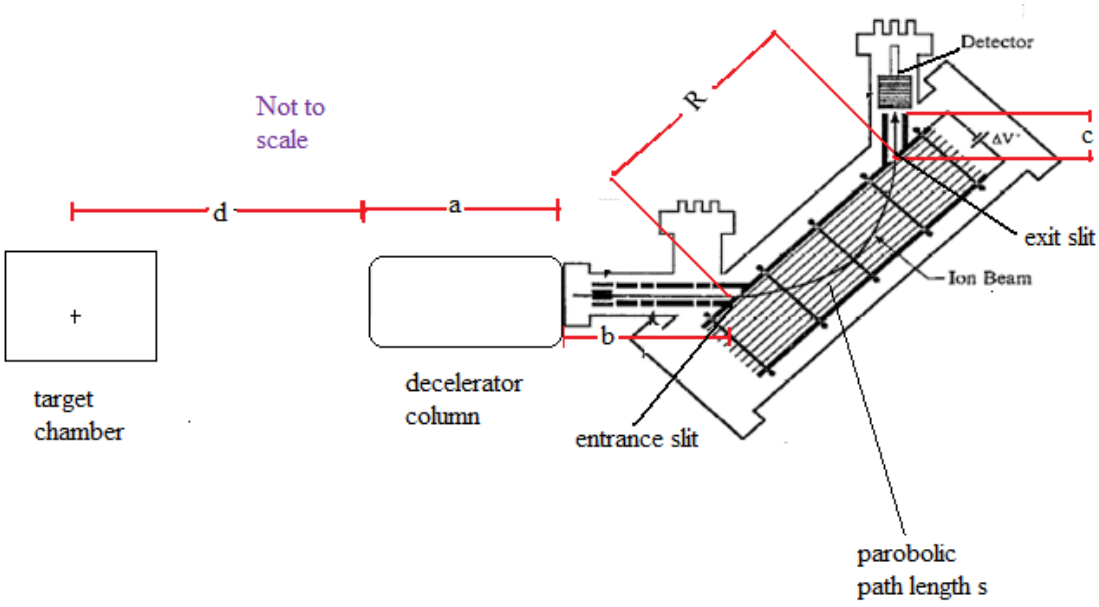

Figure 4.3. Distances related to geometric calibration. Values are listed in Table 4.1. and also explained in text.

The path length through the energy analyzer, s, is given by the path integral,

$$s = \int_0^R \sqrt{1 + y'^2}\, dx \tag{32}$$

$$y = x - \frac{eU}{2md}\frac{x^2}{v_o^2 sin^2(45^\circ)} \tag{33}$$

where the x-axis is parallel to the analyzer plates and R is the distance between the entrance and exit slits. The angular acceptance of the detector, θ_{det}, is then given by,

$$z = d\theta_{det} + \frac{1}{2}(\theta_{det} + 5\theta_{det})a + (b + c + s)5\theta_{det} \tag{34}$$

or

$$\theta_{det} = \frac{z}{3a+d+5(b+c+s)} \tag{35}$$

where z is the total deflection of the projectile on the detector. The factor of 5 in Eq. (34) in both the first and second terms accounts for the angular spread resulting from deceleration of the scattered beam to 5 keV. The total angular acceptance of the detector is then, approximately 4.56 mrad, which corresponds to an angular calibration factor of 0.015 mrad/channel. This result agrees within 3% with the calibration using helium data, well within the uncertainty of the length measurements.

4.4 NORMALIZATION

Once the calibration factor was known, the data were examined to ensure that the angular distribution was symmetric about the maximum. This symmetry allowed the data to be folded in order to bring down the statistical error bars. The data represents a double differential rate, $\frac{d^2N}{d\Omega_p dE_e}(\theta_p, E_e)$, which is proportional to the double differential cross-section. The constant of proportionality, the normalization constant, was found by equating the measured data, integrated over all projectile scattering angles and ejected electron energies, to the recommended total ionization cross-section, $\sigma(E_e)$ [64, 65]

$$\sigma(E_e) = 2\pi \int \frac{d^2\sigma}{d\Omega_p dE_e} \sin\theta d\theta dE_e = 2\pi F \int \frac{d^2N}{d\Omega_p dE_e} \sin\theta d\theta dE_e \qquad (36)$$

Thus the normalized double differential cross-sections $d^2\sigma/d\Omega_p dE_e$ (DDCS) were obtained, differential in Ω_p, the projectile solid angle, and E_e, the ejected electron energy, as a function of the polar projectile scattering angle θ_p, for fixed projectile energy loss ΔE, corresponding to fixed ejected electron energy.

5. RESULTS AND DISCUSSION

5.1 OVERVIEW

In this chapter, doubly-differential cross-sections $d^2\sigma/d\Omega_p dE_e$ (DDCS), where Ω_p is the projectile solid angle, and E_e is the ejected electron energy, are presented as a function of the polar projectile scattering angle for fixed projectile energy losses of 30, 50, 53, 57, 65, and 70 eV. Pronounced structures are observed directly in these cross-sections at large scattering angles for energy losses of 30, 50, and 70 eV without having to normalize to atomic cross-sections. These large angle structures are further analyzed by taking the ratio of the experimental data with twice the theoretical atomic hydrogen cross-sections, calculated using the models discussed in Chapter 2. By comparing the cross-sections and ratios in light of the approximations made in each model, it is demonstrated that only models that include the projectile-target nucleus interaction have even qualitative agreement with the data. This analysis indicates that the structure directly observed in the double differential cross-section as a function of projectile scattering and ejected electron energy is due to interference in the scattered projectile wave-function resulting from the coherent interaction with the two scattering centers of the molecule. In addition, the molecular orientation has been estimated from the data and provides the first experimental evidence that the ionization process in charged particle impact is dependent on the molecular orientation. For large scattering angles, a longitudinal orientation is preferred, while a transverse orientation is preferred for small scattering angles. This estimated molecular orientation for fixed scattering angle was included in a CDW-EIS (Continuum Distorted Wave-Eikonal Initial State) calculation and excellent agreement with the data is demonstrated.

5.2. DOUBLY-DIFFERENTIAL CROSS-SECTIONS

In Figure 5.1 the doubly-differential cross-sections $d^2\sigma/d\Omega_p dE_e$ (DDCS) for single ionization of molecular hydrogen by 75 keV proton impact for fixed projectile energy losses of 30, 50, 53, 57, 65, and 70 eV are plotted as a function of the projectile scattering angle (closed circles). Error bars represent one standard deviation from the mean. For comparison, a typical atomic cross-section is presented for helium (open circles in Figure 5.1). Such cross-sections decrease rapidly as a function of increasing scattering angle and show no structure. The molecular cross-sections follow the general trend of an atomic cross-section, rapidly decreasing as a function of increasing scattering angle. However, for large scattering angles, near 1.2 mrad, prominent structures are observed for energy losses of 30 and 50 eV and again for 70 eV. At energy losses near 57 eV the large angle structure disappears. First, the large angle structures will be analyzed further. The disappearance of this structure at an energy loss of 57 eV will then be discussed in Section 5.4. As discussed in Chapter 4, the background was eliminated by setting a condition on the TAC spectrum and subtracting random coincidences. However, in principle one could argue that the random subtraction is not perfect. The DDCS at large angle for energy losses ΔE, where no structure is observed, provide an upper limit for the background contribution. Those DDCS are consistently at the level of $1x10^{-14}$ $cm^2/sr*eV$ or smaller. On the other hand, the DDCS where large angle structures appear are at least at the level of $5x10^{-14}$ $cm^2/sr*eV$ and as large as $2x10^{-13}$ $cm^2/sr*eV$ for small energy loss. Therefore, it is clear that any possible imperfections in the random subtractions do not rise even near the level of the DDCS where large angle structures appear.

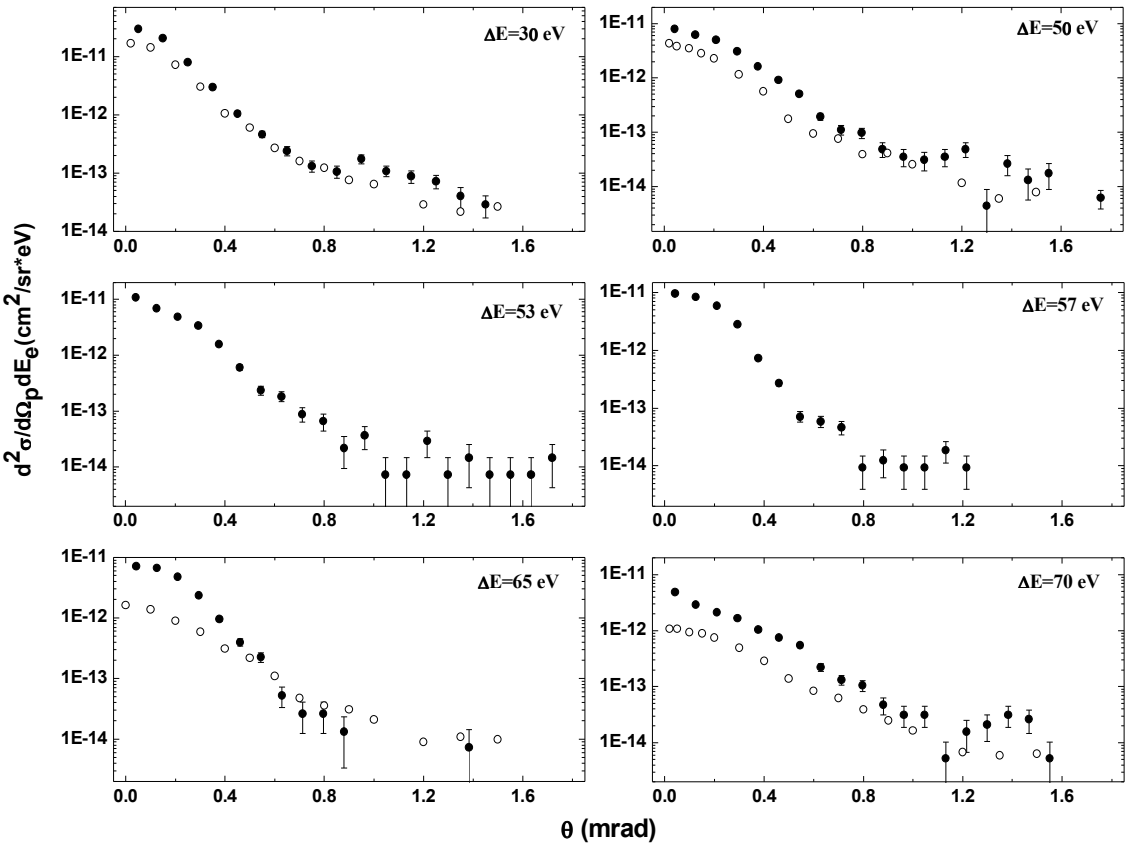

Figure 5.1. Double differential cross-sections as a function of scattered projectile angle for energy losses of 30, 40, 50, 53, 57, 65, and 70 eV (closed circles). Atomic helium cross-sections (open circles).

In order to further analyze the large-angle structure in Fig. 5.1 the ratios, R, between the measured DDCS for H_2 and twice the theoretical DDCS for atomic hydrogen (closed circles) for energy losses of 30, 50, 57, and 70 eV are presented in Figure 5.2. The theoretical cross sections were calculated using the continuum distorted wave–eikonal initial state (CDW-EIS) approach including the projectile–residual target ion (PI) interaction as discussed in Section 2.2. The structures already observed in the cross-sections of Figure 5.1 become even more prominent in the ratios, R, and a second structure at smaller angles (around 0.3 mrad) becomes visible. Correspondingly, the complete absence of the structure at large scattering angles around an energy loss of 57 eV is more evident in the ratios as well. As shown in Section 2.4, the triple differential cross-section (TDCS) averaged over all molecular orientations can be written as,

$$TDCS_{H2} = 2*TDCS_{H}\,(1 + \sin\chi/\chi) \qquad (37)$$

where $\chi = p_{rec}D$, p_{rec} is the magnitude of the recoil-ion momentum and D is the inter-nuclear distance in the molecule. The recoil-ion momentum, the magnitude of which enters in χ, is given by $\mathbf{p_{rec}} = \mathbf{q} - \mathbf{k_e}$. The double differential ratios in Figure 5.2 can therefore be viewed as the interference term, $1+\sin\chi/\chi$, averaged over all recoil-ion momenta $\mathbf{p_{rec}}$ and molecular orientations. As discussed in Section 1.1, it was assumed by Stolterfoht et al. [10, 11] that the double differential electron energy spectra are dominated by collisions with small momentum transfer **q**, so that in those cross-sections the interference pattern is determined by the ejected electron momentum spectra.

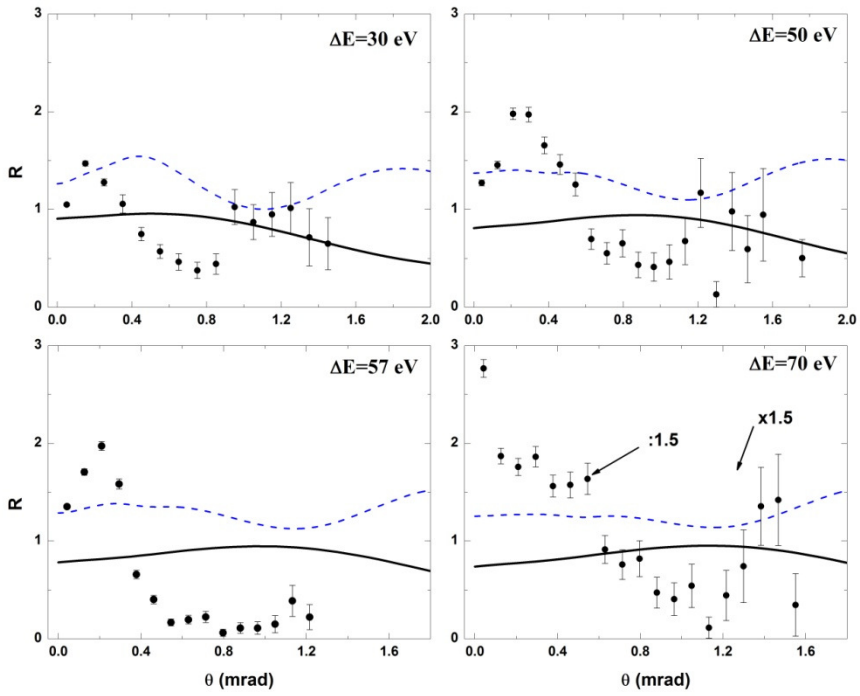

Model	Projectile-target nucleus	Post-Collision Interaction	Molecular Orientation
FBA-PCI	Not included	Included	Averaged
CDW-EIS	Included	Included	Averaged

Figure 5.2. Ratios, R, between experimental and theoretical molecular DDCS and twice the theoretical DDCS for atomic hydrogen plotted as a function of the projectile scattering angle for fixed energy losses of 30, 50, and 70 eV, respectively. Solid black curves – FBA-PCI, Blue dashed curves – CDW-EIS calculation.

Here, interference maxima are observed at scattering angles larger than 1 mrad corresponding to momentum transfers of larger than 3 to 3.5 a.u. (depending on ΔE), while the electron momentum ranges from 1 to 2 a.u.

It should be noted that the large angle structure cannot be associated to binary projectile-electron scattering (Bethe ridge) [66, 27]. Because the maximum scattering angle for a proton from an electron at rest is $M_e/M_p \sim 0.55$ mrad, this process does not occur at larger scattering angles. Therefore, as pointed out by Salin [67], the large-angle deflection of the protons is mostly due to the projectile-target nucleus interaction (except for large projectile energies) If we now consider, as described in Section 2.4, that we have a molecule composed of *two* scattering centers, the resulting scattering amplitudes must be added coherently. Therefore, the occurrence of interference maxima at large scattering angles in DDCS as a function of the projectile scattering angle clearly suggests that the interaction between the projectile and the residual target ion (PI) plays a critical role in the interference pattern.

5.3. COMPARISON TO THEORY

The solid black curves in Fig. 5.2 represent a calculation utilizing the FBA-PCI theory of Section 2.2. Recall that the post-collision interaction (PCI) between the scattered projectile and the ejected electron is accounted for in an ad hoc manner in this model using the modified Gamow factor of Salin [33, 34, 35]. However, the projectile-target nucleus interaction (PI) is not included at all since the projectile is treated as a plane wave in this model and the electronic initial and final state wave-functions are orthogonal. The FBA-PCI calculation is in poor agreement with the data for all energy losses.

In contrast, the CDW-EIS calculation (blue curves) [18, 21, 23] includes both PCI and the PI interaction. Effective charges, both in the initial (Zeff=$\sqrt{2 * \epsilon_i}$ where ϵ_i=0.566 au, the first ionization potential of H_2) and final (Zeff= 1.193) electronic states, were used in order to account for the presence of the "passive" remaining electron in the H_2 molecular target. Qualitatively, better agreement with the data is achieved than with FBA-PCI calculation to the extent that a structure with two maxima is reproduced by the CDW-EIS calculation. However, the quantitative agreement is not yet very good. The distance between the maxima for the H_2 DDCS is also in good qualitative agreement with experiment, however the entire interference pattern is systematically shifted towards larger angles in the calculation and is less pronounced than in the data. The CDW-EIS calculation of the DDCS for the atomic helium target reproduces both a calculation employing the same model [47] and measured data [30]. In contrast to the molecular case, the calculation does not yield any structures for atomic helium, in agreement with the experimental data. If the PI interaction is removed from the CDW-EIS model for H_2, similarly poor agreement as with the FBA-PCI calculation is obtained. This strongly supports the contention that the PI interaction is needed in the theory in order to obtain even qualitative agreement with the data.

The integration over the molecular orientation, which leads to Eq. (37) is based on the assumption that each orientation of the molecule contributes equally to the ionization amplitude. However, it is not evident that this approximation is valid. An estimate of the validity of this approximation can be obtained from the data. Assuming that for each scattering angle there is a preferred fixed molecular orientation ϕ, the interference term $\mathcal{I}$ becomes $\mathcal{I}$ = (1 + cosχ), instead of 1+sinχ/χ, where now $\chi = \mathbf{p_{rec}} * \mathbf{D} = p_{rec} * D * \cos\alpha$

[17]. Here, α is the angle between $\mathbf{p_{rec}}$ and **D.** Triple differential measurements [28, 29] for 75 keV p + He show that for a fixed scattering angle and electron energy, as is the case in the present cross-sections, the direction of the ejected electrons is well determined within a narrow angular range. Since $\mathbf{p_{rec}} = \mathbf{q} - \mathbf{k_e}$, $\mathbf{p_{rec}}$ is also well determined and a good estimate of the molecular orientation can be obtained from the double differential data. Assuming that the recoil-ion momentum distribution for atomic hydrogen is similar to helium and using this distribution along with the measured ratios from Fig. 5.2, ϕ (which contains α and the recoil-ion direction) can be deduced from $R = 1 + \cos(p_{rec}*D*\cos\alpha)$. These estimated ϕ are plotted in Figure 5.3 as a function of projectile scattering angle for energy losses of 30, 50, and 70 eV. It is quite evident that for small scattering angles a transverse orientation (i.e. $\phi \approx 90^o$) and for large scattering angles a longitudinal orientation (i.e. $\phi \approx 0^o$) is preferred. In contrast, no significant differences between the data sets for different energy losses can be identified. Therefore, even after integrating over the electron energy, the molecular orientation remains essentially frozen for a fixed scattering angle, while integration over the scattering angle leaves ϕ undetermined, even for fixed electron energy. This suggests why the interference pattern is more pronounced in the projectile scattering angle dependence than in the electron energy dependence of the DDCS and that in the CDW-EIS calculation the structures are less pronounced than in the data. The solid red curves in Figures 5.4 and 5.5 are CDW-EIS calculations for molecules with a fixed orientation obtained from Figure 5.3. For the fixed orientation, the calculations are in excellent agreement with the data at 30 and 50 eV.

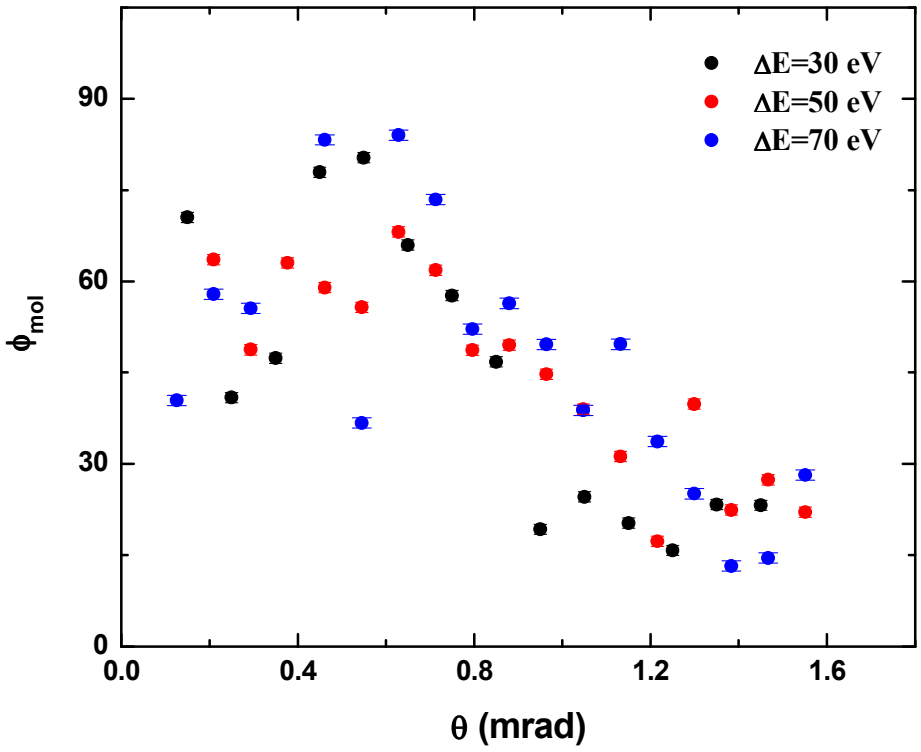

Figure 5.3. Estimated molecular orientation ϕ as a function of projectile scattering angle for energy losses of 30, 50, and 70 eV.

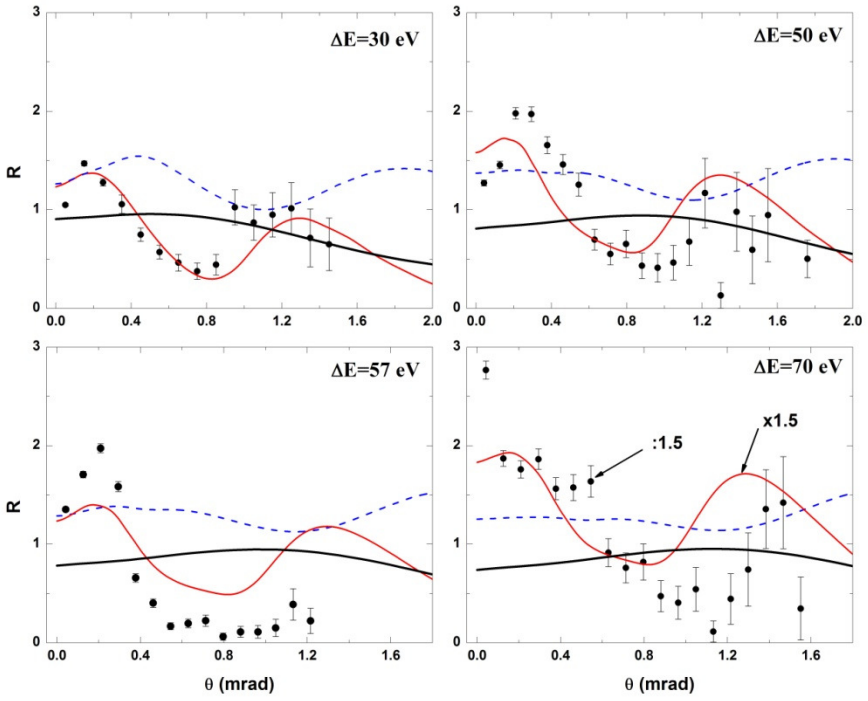

Model	Projectile – target nucleus	Post-collision interaction	Molecular Orientation
FBA-PCI	Not included	Included	Averaged
CDW-EIS	Included	Included	Averaged
CDW-EIS	Included	projectile-residual target ion interaction, post-collision interaction	Fixed for a given scattering angle; changes w/scattering angle

Figure 5.4. DDCS ratios, R, plotted as a function of the projectile scattering angle for fixed energy losses of 30, 50, and 70 eV, respectively. Blue dashed curves – CDW-EIS calculation; solid red curves – CDW-EIS calculation with fixed molecular orientation.

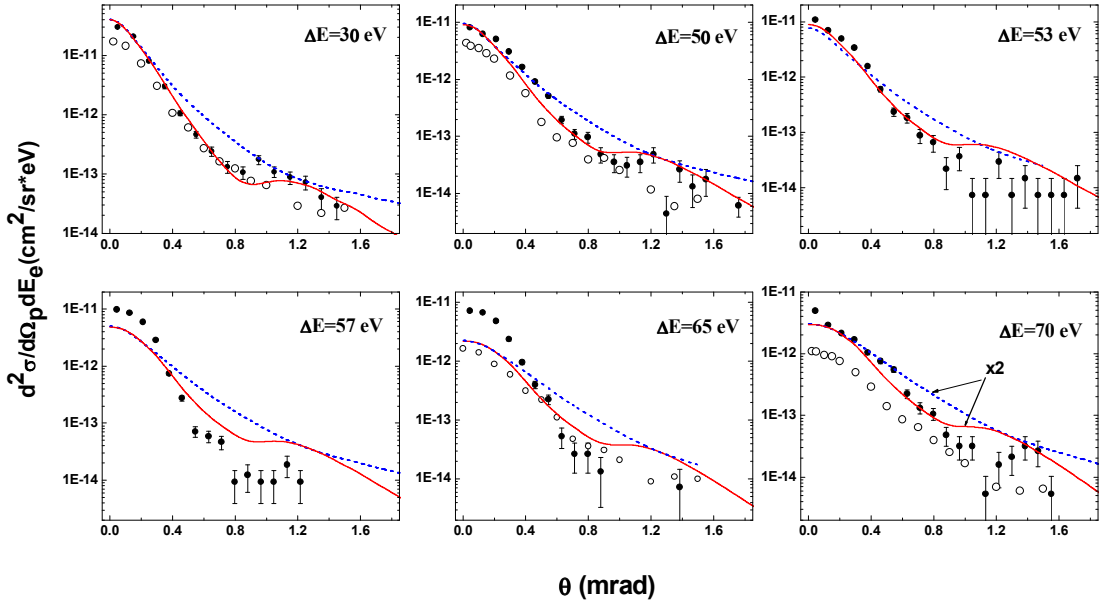

Figure 5.5. DDCS plotted as a function of the projectile scattering angle for fixed energy losses of 30, 50, 53, 57, 65, and 70 eV, respectively. Blue dashed curves – CDW-EIS calculation; solid red curves – CDW-EIS calculation with fixed molecular orientation.

Furthermore, much better agreement is achieved with the shape of the data both directly in the DDCS and in the ratios for all energies, including 57 eV, than the calculation using averaged orientations (blue curves). The magnitudes are generally well reproduced, as well. Only at 70 eV do both calculations underestimate the data by about a factor of two. A similar trend has been observed for a helium target, although, as mentioned above, CDW-EIS calculations are in overall nice agreement with experimental data for 75 keV proton impact. At other projectile energies, both below and above 75 keV, there is a tendency for this model to underestimate the DDCS at large energy losses [47]. The discrepancy in magnitude for H_2 at 70 eV therefore does not appear to necessarily be related to the description of molecular effects.

5.4. DISAPPEARANCE OF LARGE ANGLE STRUCTURE

At an energy loss of 57 eV the ejected electron speed is the same as the projectile speed. The post-collision interaction (PCI) between these two particles is known to maximize for this electron to projectile speed [30]. The post-collision interaction between the scattered projectile and the ejected electron is a well-known effect, previously studied in the single ionization of helium by proton impact [30]. In the DDCS as a function of scattering angle, PCI leads to a narrowing of the angular distribution, as seen in Figure 5.5 below and previously observed for a helium target [30].

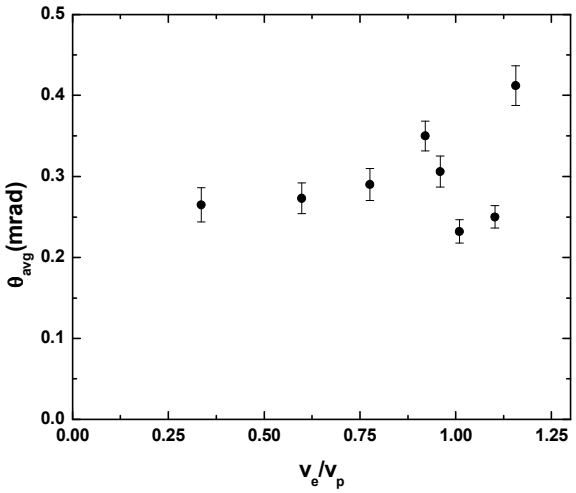

Figure 5.6. Average scattering angle as a function of the ratio of the ejected electron speed to the projectile speed.

In Figure 5.6 the average scattering angle,

$$\theta_{avg} = \frac{\int \frac{d^2\sigma}{dE_e d\theta}\theta d\theta}{\frac{d\sigma}{dE_e}} \tag{38}$$

is plotted as a function of the ratio of the ejected electron to projectile velocity. This follows a general trend of increasing slope with increasing velocity ratio. However, at a ratio of approximately one, indicating the projectile and ejected electron leave the collision region with the same speed a pronounced minimum is observed. This ejected electron speed corresponds to a projectile energy loss of 57 eV, where the large angle structure in the DDCS of Figures 5.1, 5.4, and 5.6 disappears. Therefore, it appears likely that PCI is responsible for the disappearance of the large angle structure at the energy loss where this effect is a maximized.

Preliminary fully differential cross-sections at an energy loss of 57 eV [68], collected simultaneously with the double-differential cross-sections presented in this work, have been analyzed by selecting recoil-ion momentum which favor or suppress PCI. These FDCS have demonstrated that the structure at large angle scattering does indeed reappear when PCI is suppressed.

6. CONCLUSIONS AND OUTLOOK

6.1. CONCLUSIONS

The underlying motivation for the experiment described in this dissertation has been to gain further insight into few-body dynamics and to provide a sensitive test of theoretical models. This has been accomplished through the study of interference effects in ionization of molecular hydrogen by intermediate energy ion impact. Double differential cross-sections $d^2\sigma/d\Omega_p dE_e\,(\theta, \Delta E)$, where Ω_p is the projectile solid angle and E_e is the ejected electron energy, have been measured for single ionization of molecular hydrogen by 75 keV proton impact. This was accomplished by detecting the scattered momentum analyzed projectile in coincidence with the recoil ion.

Well-defined structures have been observed directly in the DDCS for large scattering angles around approximately 1.2 mrad, without any normalization to atomic cross-sections. These large angle structures were further analyzed by taking the ratio of the experimental data with twice the theoretical atomic hydrogen cross-sections, calculated, using the models discussed in Chapter 2. In these ratios, the large angle structure observed directly in the DDCS becomes even more pronounced and a second structure at a smaller scattering angle, around 0.3 mrad, becomes evident.

In addition, the molecular orientation has been estimated from the data and this analysis provides the first experimental evidence that the ionization process in single ionization by charged particle impact is dependent on the molecular orientation. For large scattering angles, a longitudinal orientation is preferred, while a transverse orientation is preferred for small scattering angles. This estimated molecular orientation for fixed scattering angle was included in a CDW-EIS calculation and excellent

agreement with the data has been demonstrated, both in the ratios and directly in the DDCS, If, in contrast, the projectile-target nucleus interaction is not included or if the calculation is averaged over all molecular orientations, the agreement with the data is very poor. Therefore, it is concluded that the structure in the DDCS is due to a previously unobserved interference in the scattered projectile wave-function.

Previously, Stolterföht et al [10] attributed structures in double differential electron energy spectra for fixed emission angles to an interference in the ejected electron wave [11]. A critical assumption in that analysis was that the momentum transfer is small. In the present experiment this assumption is clearly not justified since the observed structures occur at angles corresponding to $q>>k_e$. Therefore, the interpretation in [10] would be questionable for the current case. However, even for the work of [10] the assumption $q<<k_e$ should be reconsidered. This assumption ignores the projectile-target nucleus interaction completely, which is quite important for 60 MeV/u Kr^{34+} collisions because of the large projectile charge.

Although the role of PCI could not be definitively established in this work, it appears to play a crucial role in eliminating the interference structure when v_e approaches v_p.

6.2 OUTLOOK

6.2.1. Fully Differential Cross-Sections. As indicated in Section 5.4, fully differential cross-sections have been extracted from the present raw experimental data at an energy loss of 57 eV [68]. A preliminary analysis of these FDCS by selecting recoil-ion momentum that favor or suppress PCI demonstrates that the structure at large angle

scattering in Figures 5.1, 5.1, and 5.3 does indeed reappear when PCI is suppressed. This supports the conclusion that the post-collision interaction between ejected electron and scattered projectiles leads to a focusing of the angular distribution of the ionization cross-section at an energy loss where the ratio of the ejected electron speed to the projectile speed is nearly one. The recoil-ion momentum resolution was not optimized during the collection of these data (see Figure 3.5). As demonstrated in the recoil-ion position spectrum in Figure 6.1 the recoil-ion momentum resolution has since been improved the as the ionization and capture lines are now well defined. A new experiment is therefore under way to measure FDCS [68].

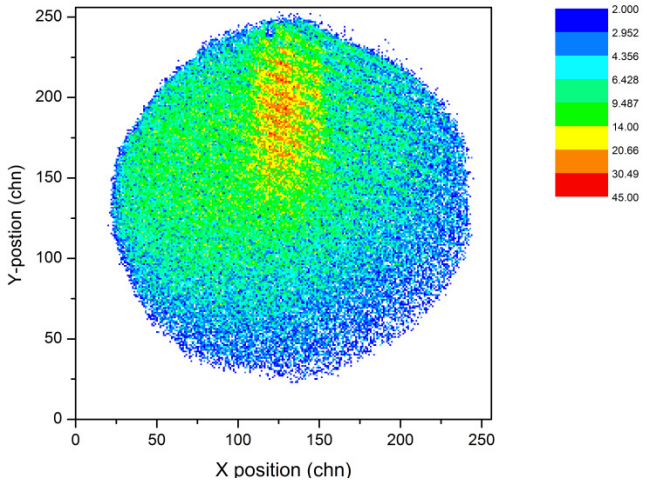

Figure 6.1 Recoil-ion position spectrum showing improved momentum resolution.

In addition to the measurement of FDCS presently underway, with a multi-hit detector, which can differentiate the event from two (or more) charged particles simultaneously hitting the detector, could be used to verify the estimates of the molecular orientation of the present work by measuring the fragmentation energy of recoiling

protons in dissociative ionization. This has recently been done with capture experiments using H_2 as a target [69].

6.2.2. Other Possible Molecular Targets. Although H_2 is the simplest neutral molecular system, other molecular target/projectile systems should exhibit similar interference structures in the single ionization cross-sections as a function of the projectile scattering angle and ejected electron energy. Based on a simple geometrical argument comparing the de Broglie wavelength of the projectile and the equilibrium spacing of the molecule, Table 6.2 lists estimates of the probable location of interference structures in the DDCS for single ionization of these molecules by 75 keV proton impact.

Molecule	Ground State	Minima (mrad)	Internuclear separation D (au)
N_2	$^1\Sigma^+g$	0.95	2.07
O_2	$^3\Sigma^+g$	0.82	2.41
NO	$^2\Pi i$	0.91	2.17
NH	$^2\Sigma^+$	1.02	1.94
OH	$^2\Pi$	1.06	1.85
CO	$^1\Sigma^+$	0.93	2.13
HF	$^1\Sigma^+$	1.14	1.73
LiH	$^1\Sigma^+$	0.66	3.02
Li_2	$^1\Sigma^+g$	0.39	5.08
H_2	$^1\Sigma^+g$	1.41	1.40

Table 6.1. Estimates of the probable location, in terms of the projectile scattering angle, of interference minima in the DDCS for single ionization of various molecular targets by 75 keV proton impact.

These estimates are based entirely on the analogy to the optical case in which $m\lambda = \mathrm{D}\sin(\mathbf{p}_{\mathrm{rec}} \cdot \mathbf{D})$, where in this case $\lambda=h/p_o$ is the de Broglie wavelength of the incident projectile, p_o is the initial projectile momentum, and D is the equilibrium internuclear spacing of the molecule. If the kinematic conditions are chosen such that $\mathbf{k}_e \ll \mathbf{q}$, (i.e. for small ΔE and large θ) as in the present experiment, then $\mathbf{p}_{rec}=\mathbf{q}-\mathbf{k}_e \sim \mathbf{q}$ and the phase angle above becomes mainly dependent on $p_o\sin(\theta_p)$.

Clearly, these molecular targets present an even greater challenge to theory as the additional passive electrons in the molecule must be accounted for. Experimentally, difficulties would be encountered as well e.g. production of cold beams of Li_2, LiF, NH, HF, and NO require special techniques.

Finally, it is clear both from the present experimental results and from the possible extensions of the investigation of interference effects in the scattered projectile wave-function described briefly above, that the present work represents a significant contribution to the specific line of inquiry regarding interference phenomena in ionizing collisions, in particular regarding the interference in the scattered projectile wave-function. More generally, the present work provides a sensitive test of theoretical models leading to greater insight into few-body dynamics.

BIBLIOGRAPHY

[1] M.A. Morrison, *The Joy of Quantum Physics*, Princeton University Press, Princeton, New Jersey (2009).

[2] T. N. Rescigno, M. Baertschy, W. A. Issacs, and C. W. McCurdy, Science **286** 2474 (1999)

[3] M. Schulz, R. Moshammer, D. Fischer, H. Kollmus, D. H. Madison, S. Jones, and J. Ullrich, Nature **422** 48 (2003)

[4] M. Schulz and D. H. Madison, Int. J. Mod. Phys. A **21** 3649 (2006)

[5] R. Dörner, V. Mergel, O. Jagutzki, L. Spielberger, J. Ullrich, R. Moshammer and H. Schmidt-Böcking, Physics Reports **330** 192 (2000); J. Ullrich, R. Moshammer, R Dörner, O. Jagutzki, V. Mergel, H. Schmidt-Böcking and L. Spielberger, J. Phys. B: At. Mol. Opt. Phys. **30** 2917 (1997)

[6] M. Schulz, M. Dürr, B. Najjari, R. Moshammer, and J. Ullrich, Phys. Rev. A **76**, 032712 (2007)

[7] M. Schulz, R. Moshammer, A.N. Perumal, and J. Ullrich, J. Phys. B **35** L161 (2002)

[8] T.F. Tuan and E. Gerjoy Phys. Rev. **117** 756 (1960)

[9] D. Cohen and U. Fano Phys. Rev. **150** 30 (1966)

[10] N. Stolterfoht, B. Sulik, V. Hoffmann, B. Skogvall, J. Y. Chesnel, J. Rangama, F. Frémont, D. Hennecart, A. Cassimi, X. Husson, A. L. Landers, J. A. Tanis, M. E. Galassi, and R. D. Rivarola Phys. Rev. Lett. **87** 023201 (2001)

[11] N. Stolterfoht, B. Sulik, L. Gulyás, B. Skogvall, J. Y. Chesnel, F. Frémont, D. Hennecart, A. Cassimi, L. Adoui, S. Hossain, and J. A. Tanis, Phys. Rev. A **67**, 030702 (2003)

[12] S. Hossain, A. S. Alnaser, A. L. Landers, D. J. Pole, H. Knutson, A. Robison, B. Stamper, N. Stolterfoht and J. A. Tanis**,** Nuclear Instruments and Methods in Physics Research Section B: Beam Interactions with Materials and Atom**s 205** 484 (2003)

[13] D. Misra, U. Kadhane, Y.P. Singh, L.C. Tribedi, P.D. Fainstein, and P. Richard, Phys. Rev. Lett. **92**, 153201 (2004)

[14] D. S. Milne-Brownlie, M. Foster, Junfang Gao, B. Lohmann, and D. H. Madison, Phys. Rev. Lett. **96**, 233201 (2006)

[15] E.M. Staicu Casagrande, A. Naja, F. Mezdari, A. Lahmam-Bennani, P. Bolognesi, B. Joulakian, O. Chuluunbaatar, O. Al-Hagan, D. H. Madison, D.V. Fursa and I. Bray, J. Phys. B **41**, 025204 (2008)

[16] D. Akoury, K. Kreidi, T. Jahnke, Th. Weber, A. Staudte, M. Schöffler, N. Neumann, J. Titze, L. Ph. H. Schmidt, A. Czasch, O. Jagutzki, R. A. Costa Fraga, R. E. Grisenti, R. Díez Muiño, N. A. Cherepkov, S. K. Semenov, P. Ranitovic, C. L. Cocke, T. Osipov, H. Adaniya, J. C. Thompson, M. H. Prior, A. Belkacem, A. L. Landers, H. Schmidt-Böcking and R. Dörner, Science **318,**.949 **(**2007**)**

[17] M. E. Galassi, R. D. Rivarola, and P. D. Fainstein, Phys. Rev. A **70**, 032721 (2004)

[18] M. F. Ciappina and R. D. Rivarola, J. Phys. B **41** 015203 (2008)

[19] J. H. McGuire, N. Berrah, R. J. Banlett, J. **A .**R. Samson, J. **A.** Tanis, C. L. Cocke and **A.** S. Schlachter, J. Phys. B: At. Mol. Opt. Phys. **28** 913 (1995)

[20] D. Misra, A. Kelkar, U. Kadhane, Ajay Kumar, Lokesh C. Tribedi, and P. D. Fainstein Phys. Rev. A **74**, 060701 (2006)

[21] P. D. Fainstein, L. Gulyás, F. Martín, and A. Salin, Phys. Rev. A **53**, 3243 (1996)

[22] E M Staicu Casagrande *et al* J. Phys. B: At. Mol. Opt. Phys. **41** 025204 (2008)

[23] J.S. Alexander, A.C. Laforge, A. Hasan, Z.S. Machavariani, M.F. Ciappina, R.D. Rivarola, D.H. Madison, and M. Schulz, Phys. Rev. A **78** 060701(R) (2008)

[24] J. Peacher, Course Lecture Notes: Atomic Collisions, Department of Physics, Missouri University of Science and Technology, Rolla, MO (2008)

[25] M. Mott and Massey, *The Theory of Atomic Collisions*, (Oxford Press, London 1965)

[26] A. Messiah, *Quantum Mechanics*, (Dover Series Reprint, New York 1998)

[27] M. Inokuti, Rev. Mod. Phys. **43** 297 (1971)

[28] J Berakdar, J S Briggs, and H Klar, J. Phys. B At.Mol. Opt. Phys. **26** 285 (1993)

[29] L. Gulyás, P. D. Fainstein, and A. Salin, J. Phys. B: At. Mol. Opt. Phys. **28** 245 (1995)

[30] M. Schulz, T. Vajnai, A. D. Gaus, W. Htwe, D. H. Madison, and R. E. Olson, Phys. Rev. A **54** 2951 (1996)

[31] N. V. Maydanyuk, A. Hasan, M. Foster, B. Tooke, E. Nanni, D. H. Madison, and M. Schulz, Phys. Rev. Lett. **94** 243201 (2005)

[32] M. Schulz, A. Hasan, N.V. Maydanyuk, M. Foster, B. Tooke, and D.H. Madison, Phys. Rev. A **73**, 062704 (2006)

[33] A. Salin, J. Phys. B: At. Mol. Opt. Phys. **2** 631 (1969)

[34] D. Madison and K. Bartschat, Phys. Rev. A **34** 4669 (1986)

[35] M. Brauner and J. H. Macek, Phys. Rev. A **46** 2519 (1992)

[36] B. H. Bransden and C. J. Joachain, *Physics of Atoms and Molecules*, *2nd Ed.* Pg 611, (Pearson Education, London, 2003)

[37] D. S. F. Crothers and J. F. McCann, J. Phys. B: At. Mol. Opt. Phys. **16** 3229 (1983)

[38] Chesire, Proc. Phys. Soc. **84** 89 (1964)

[39] Dž Belkić J. Phys. B: At. Mol. Opt. Phys. **11** 3529 (1978)

[40] D. S. F. Crothers, Phys. Sc. **40** 634 (1989)

[41] N. Stolterfoht, R. D. DuBois, and R. D. Rivarola, *Electron Emission in Heavy Ion Collisions*, (Springer, Berlin 1997)

[42] P. D. Fainstein, V. H. Ponce, and R. D. Rivarola, J. Phys. B: At. Mol. Opt. Phys. **24** 3091 (1991)

[43] J. Mathews and R.L. Walker, *Mathematical Methods of Physics*, W.A. Benjamin, Inc. New York (1965)

[44] M. Ciappina and W. R. Cravero, Brazilian J. Phys. **36** 524(2006)

[45] N. R. Arista, Nucl. Inst. and Methods in Phys. Res. B **164** 108 (2000)

[46] S. E. Corchs, R. D. Rivarola, J. H. McGuire and Y. D. Wang, Phys. Scr. **50** 469 (1994)

[47] V. D. Rodriguez and R. O. Barrachina, Phys. Rev. A **57** 215 (1998)

[48] Copyright Colutron Research Corporation, Boulder, Colorado, Figure reproduced with author's permission.

[49] A.D. Gaus, W. T. Htwe, J. A. Brand, T. J. Gay, and M. Schulz, Rev. Sci. Instrum. **65** 3739 (1994)

[50] J. H. Moore, C. C. Davis, M. A. Copeland, S. C. Greer, *Building Scientific Apparatus 3rd Ed*, Perseus Books, Cambridge, MA (2003)

[51] N. F. Ramsey, *Molecular Beams*, *Molecular Beams* (Oxford University Press, New York, 1955)

[52] G. Scoles, D. Bassi, U. Buck and D. C. Laine, *Atomic and Molecular Beam Methods Vol. I* (Oxford University Press, New York, 1988)

[53] Journal of Experimental and Theoretical Physics, Vol. 94, No. 2, 2002, pp. 228–238

[54] W. C. Wiley and I. H. McLaren, Rev. Sci. Inst. **26** 1150 **(**1955)

[55] J. Ullrich and V. P. Shevelko, *Many Particle Quantum Dynamics in Atomic and Molecular Fragmentation* (Springer, Berlin, 2003)

[56] J. L. Wiza, Nuc. Inst. and Methods, **162**, 587 (1979)

[57] M. Wolf, Physik in unserer Zeit 12 90 (2006)

[58] A. Gauss, Ph.D. dissertation, University of Missouri-Rolla (1994)

[59] Fiberlink Series transmitters/receivers http://www.commspecial.com

[60] P. Horowitz and W. Hill, *The Art of Electronics*, *2nd Ed.* (Cambridge University Press 1989)

[61] User Manual Ortec CF8000, Ortec Technical Services, http://www.ortec-online.com/electronics/disc/cf8000.htm

[62] G. Drake, *Handbook of Atomic, Molecular and Optical Physics*, 2nd Ed, (Springer, Berlin, 2006)

[63] K-Max v6.1 User Manual, Sparrow Corporation, 1179 Dominion Court Port Orange, FL 32129

[64] Atomic Data for Fusion, C.F. Barnett (ed.), Oak Ridge National Laboratory, D16, Oak Ridge (1990), http://www-cfadc.phy.ornl.gov/redbooks/redbooks.html

[65] U.M.E. Rudd, K. Kim, D. H. Madison and T. Gay, Rev. Mod. Phys. **64** 441 (1992)

[66] L. D. Landau and L. M. Lifschitz, *Quantum Mechanics: Non-Relativistic Theory Vol. 3* (Butterworth-Heinemann, New York, 1981)

[67] A. Salin, Phys. Rev. A 36 5471 (1987)

[68] A.C. Laforge, K. Egodapitiya, J. S. Alexander, D.H. Madison and M. Schulz, in preparation

[69] F. Rosca-Pruna and M. J. J. Vrakking Phys. Rev. Lett. **87** 153902 (2001)

VITA

Jason Shane Alexander was born on June 17, 1977 in Sikeston, MO. He earned a Bachelor of Science degree in Physics from Southeast Missouri State University in May 2002. In July 2006, he completed his M.S. (Thesis Option) in Physics at the University of Oklahoma. Jason will receive his Ph.D. in Physics from Missouri University of Science and Technology in May 2009 under the guidance of Professor Michael Schulz.

In September 2008 a paper based on his dissertation work was published as a Rapid Communication in Physical Review A. [23].